TWO DIMENSIONAL SILICON PHOTONIC CRYSTAL BAND GAP APPLICATIONS FOR OPTICAL BIO-SENSING AND MODULATION

A THESIS SUBMITTED TO
THE GRADUATE SCHOOL OF NATURAL AND APPLIED SCIENCES
OF
MIDDLE EAST TECHNICAL UNIVERSITY

BY

SELAHATTİN CEM KILIÇ

IN PARTIAL FULFILLMENT OF THE REQUIREMENTS
FOR
THE DEGREE OF MASTER OF SCIENCE
IN
ELECTRICAL AND ELECTRONIC ENGINEERING

SEPTEMBER 2021

Approval of the thesis:

TWO DIMENSIONAL SILICON PHOTONIC CRYSTAL BAND GAP APPLICATIONS FOR OPTICAL BIO-SENSING AND MODULATION

submitted by **SELAHATTİN CEM KILIÇ** in partial fulfillment of the requirements for the degree of **Master of Science** i**n Electrical and Electronic Engineering, Middle East Technical University** by,

Prof. Dr. Halil Kalıpçılar
Dean, Graduate School of **Natural and Applied Sciences** _____

Prof. Dr. İlkay Ulusoy
Head of the Department, **Electrical & Electronics Eng.** _____

Assoc. Prof. Dr. Serdar Kocaman
Supervisor, **Electrical & Electronics Eng.** _____

Examining Committee Members:

Prof. Dr. Gönül Turhan Sayan
Electrical and Electronics Eng, METU _____

Assoc. Prof. Dr. Serdar Kocaman
Electrical and Electronics Eng, METU _____

Prof. Dr. Barış Bayram
Electrical and Electronics Eng, METU _____

Assoc. Prof. Dr. Selçuk Yerci
Electrical and Electronics Eng, METU. _____

Assoc. Prof. Dr. Mirbek Turduev
Electrical and Electronics Eng, TED University _____

Date: 09.09.2021

I hereby declare that all information in this document has been obtained and presented in accordance with academic rules and ethical conduct. I also declare that, as required by these rules and conduct, I have fully cited and referenced all material and results that are not original to this work.

Name Last name: Selahattin Cem Kılıç

Signature:

ABSTRACT

TWO DIMENSIONAL SILICON PHOTONIC CRYSTAL BAND GAP APPLICATIONS FOR OPTICAL BIO-SENSING AND MODULATION

Kılıç, Selahattin Cem
Master of Science, Electrical and Electronic Engineering
Supervisor: Assoc. Prof. Dr. Serdar Kocaman

September 2021, 86 pages

In this thesis, we presented mainly two applications that utilize two dimensional Silicon photonic crystals. One application is an optical refractive index based gas/bio-sensor. The device is constructed by rod-type square lattice photonic crystal cavity. The rod-type is chosen to confine the electric field in the low-index medium and maximize the light-matter interaction. The resonance characteristics is selected as Fano-like resonance due to its sharp and asymmetric shape that is suitable for such an application. The rods are sandwiched between two metal plates so that the out-of-plane light confinement is achieved by reflection. First the theory of the design is described and numerical analysis and characterization of the device is conducted. An air gap is introduced on top of the rods which acts like a slot structure to confine the light a spatially small region, decreasing the mode-volume and also increasing the sensitivity by amplifying light-matter interaction further. By introducing an internal tuning mechanism the size of the air gap is externally controlled by an electrical signal. This results in the resonance frequency of the device is externally controlled so that the design is highly suitable for different operation regions, environmental and fabrication errors. Another application is the experimental confirmation of a two dimensional photonic crystal Mach-Zehnder interferometer that is being utilized as

an optical modulator. The modulation is done by optical carrier injection method by utilizing plasma dispersion effect and taking advantage of the negative refractive index phenomenon which achieves a much smaller phase-shifter length compared to the similar devices in the literature.

Keywords: Photonic Crystals, Refractive Index Sensing, Resonance Cavity, Optical Modulation

ÖZ

OPTİK MODULASYON VE BİYO-TESPİT UYGULAMALARI İÇİN İKİ BOYUTLU SİLİKON FOTONİK KRİSTAL BAND AÇIKLIĞI YAPILARI

Kılıç, Selahattin Cem
Yüksek Lisans, Elektrik ve Elektronik Mühendisliği
Tez Yöneticisi: Doç. Dr. Serdar Kocaman

Eylül 2021, 86 sayfa

Bu tezde, esas olarak iki boyutlu Silikon fotonik kristalleri kullanan iki uygulama sunduk. Birinci uygulama, optik kırılma indeksi tabanlı bir gaz/biyo-sensördür. Cihaz, çubuk tipi kare yapılı fotonik kristal ile yapılmıştır. Çubuk tipi, elektrik alanını düşük indeksli ortamda muhafaza etmek ve ışık-madde etkileşimini en üst düzeye çıkarmak için seçilmiştir. Rezonans tipi olarak böyle bir uygulamaya uygun keskin ve asimetrik şekli nedeniyle Fano tipi rezonans seçilmiştir. Çubuklar iki metal plaka arasına sıkıştırılmıştır, böylece düzlem dışı ışık korunumu yansıma yoluyla elde edilmiştir. İlk olarak tasarımın yapılması için arka plan teorisini anlattık ve cihazın sayısal analizi ve karakterizasyonunu yaptık. Çubukların üzerine, ışığı uzamsal olarak küçük bir bölgeyle sınırlamak için bir yarık yapısı gibi davranan, mod hacmini azaltan ve ayrıca ışık-madde etkileşimini daha da güçlendirerek duyarlılığı artıran bir hava boşluğu ekledik. Dahili bir ayarlama mekanizmasının yaratılmasıyla, hava boşluğunun boyutu, bir elektrik sinyali ile kontrol edilebilmektedir. Bu, tasarımın farklı çalışma bölgeleri, çevre ve üretim hataları için son derece uygun olması için cihazın rezonans frekansının kontrol edilmesine imkan vermektedir. Diğer bir uygulama, optik modülatör olarak kullanılan iki boyutlu bir fotonik kristal Mach-Zehnder interferometresinin deneysel doğrulamasıdır.

Modülasyon, plazma dispersiyon etkisinden yararlanılarak ve literatürdeki benzer cihazlara kıyasla çok daha küçük bir faz kaydırıcı uzunluğu elde eden negatif kırılma indeksi olgusundan yararlanılarak optik taşıyıcı enjeksiyon yöntemiyle yapılır.

Anahtar Kelimeler: Fotonik Kristaller, Kırılma İndisi Algılama, Rezonans Boşluğu, Optik Modülasyon

To my family & my family ~~

ACKNOWLEDGMENTS

Firstly, I would like to thank my advisor Prof. Serdar Kocaman for his immense patience and relentless guidance. With his suggestions and out-of-the-box way of thinking, he truly impressed me and helped me a lot with our studies. With his supervision I have managed to experience, what I believe a fruitful Master's years with both theoretical and experimental outcomes and publications.

I want to thank Prof. Gönül Turhan Sayan, Prof. Barış Bayram, Prof. Selçuk Yerci and Prof. Mirbek Turduev for accepting to attend my thesis committee.

In addition, I also want to thank Prof. Emre Yüce for his guidance on the experimental setup and suggestions regarding to it.

During my studies, one of the main motivators were also my friends in our lab environment, Mertcan Erdil and Cem Şahiner. Their curiosity and academically-oriented way of thinking inspired me a lot, also they always had my back when I asked for help or suggestions even though Cem Şahiner is not a member of our group.

Finally, I would also like to express my gratitude to my family for their endless support and guidance. I am very lucky to have my family. I am proud of them and I hope that they are proud of me.

During this study, I acknowledge the financial support of TUBITAK BIDEB 2210-A 2019/1 Scholarship Program and TUBITAK ARDEB with project id 116E738.

TABLE OF CONTENTS

ABSTRACT v
ÖZ vii
ACKNOWLEDGMENTS x
TABLE OF CONTENTS xi
LIST OF TABLES xiii
LIST OF FIGURES xiv
LIST OF ABBREVIATIONS xviii
LIST OF SYMBOLS xix
1 INTRODUCTION 1
1.1 Gas and Bio-Sensing 2
1.2 All Optical Switching and Modulation 2
1.3 The Scope of the Thesis 4
1.4 Organization of the Thesis and Thesis Contribution 5
2 BACKGROUND INFORMATION 7
2.1 Electromagnetics Background 7
2.1.1 Maxwell's Equations and Wave Equation 8
2.1.2 Propagation of Light in Periodic Media and Photonic Crystals 10
2.1.3 Photonic Band Gaps 13
2.2 Analysis of Photonic Crystals 14
2.2.1 One-dimensional PhCs 15

2.2.2 Two-dimensional PhCs 18
2.2.3 Three-dimensional PhCs 20
2.3 Localization of Light in PhCs 21
3 HIGHLY SENSITIVE AND TUNABLE FANO-LIKE ROD-TYPE SILICON PHOTONIC CRYSTAL REFRACTIVE SENSOR 29
3.1 Two-Dimensional PhC Cavity 29
3.2 Performance Metrics 33
3.2.1 Q-Factor 33
3.2.2 Sensitivity (S) 33
3.2.3 Mode Volume (V_m) 34
3.3 Design of the Device and Numerical Analyses 34
3.3.1 FDTD and Band Gap Analyses 34
3.3.2 Insertion of Air-Gap and FEM Analyses 45
3.3.3 Replacing PEC Plates with Gold 49
3.3.4 The Tuning of the Device 51
3.3.5 Electrostatic Actuation of the Two Metal Plates 54
4 EXPERIMENTAL VERIFICATION OF OPTICAL EXCITATION FOR PHC MACH-ZEHNDER INTERFEROMETER 57
4.1 2D PhC Mach-Zehnder Interferometer Based Modulator 57
4.1.1 Numerical Analysis 59
4.2 Experimental Setup 62
4.2.1 Fabrication and Measurements 66
5 CONCLUSION AND FUTURE OUTLOOK 73
REFERENCES 77

LIST OF TABLES

TABLES

Table 3.1 Comparison of Lorentzian and Fano-Like resonance type devices 39
Table 3.2 Performance Metrics of the device with PEC plates (without gap insertion) 44
Table 3.3 Resonance Wavelength, Q-factor and extinction ratio variations for various gap sizes 53
Table 4.1. List of active components and their models that were used for experimental characterization 63
Table 5.1 Comparison of Device Performance Metrics with Literature 74

LIST OF FIGURES

FIGURES

Figure 2.1. The electromagnetic wave spectrum 8
Figure 2.2. Representation of Photonic Crystals. **(a)**, **(b)**, **(c)** are one dimensional, two dimensional and three dimensional respectively. Differing colors means different medium with varying dielectric constants. 10
Figure 2.3. Representation of a unit cell for a PhC. The parameters are listed as; *a* is the lattice constant, *r* is the hole radius and *h* is the slab thickness. 11
Figure 2.4. **(a)** SEM image of a PhC with hexagonal lattice structure in the middle of a waveguide. 220 nm Silicon wafer on 2 µm buried oxide layer patterned with Electron-beam lithography. Lattice constant and hole radius are 460 nm and 360 nm respectively. **(b)** Cross Sectional view of a unit cell. 12
Figure 2.5 Electric field confinement on periodic media with dielectric constants of 13 and 12. **(a)** The mode profile of the dielectric band mode **(b)** The mode profile of the air band mode 14
Figure 2.6. **(a)**,**(b)** Illustration of one-dimensional PhC. **(a)** Isometric view. **(b)** Top view. **(c)** Band diagram of one-dimensional PhC. 17
Figure 2.7. **(a)** Illustration of two-dimensional PhC. **(b)** Band diagram of two-dimensional PhC. Blue bands are for TE modes and red bands are for TM modes. 19
Figure 2.8. Schematic of a Rod-Type two-dimensional PhC from top view. Red cirle indicates the removal of a single rod to create a point defect. Yellow circles indicate the removal of one row of Rods to introduce a line defect. 21
Figure 2.9. Example of a PhC waveguide. **(a)** Top view of the PhC with a linear defect. **(b)** E-field profile with the opertaion wavelength selected as the midgap wavelength. Note that the field is strongly confined in the middle of the PhC waveguide and can't penetrate inside the PhC. 23

Figure 2.10. Illustration of temporal coupled-mode theory with various structures and generic transmission spectrums. **(a)** Generic resonator model with input and output pathways shown with arrows. **(b)** Schematic of a PhC side coupled cavity. **(c)** Schematic of a PhC side coupled cavity with an additional rod in the middle of the waveguide. **(d), (e)** the generic transmission spectrums for the structures that are provided in **(b)** and **(c)** in order. 24
Figure 3.1. **(a)** Schematic of the simulated two-dimensional rod-type PhC. **(b)** The transmission spectrum of the device is shown in **(a)**. 31
Figure 3.2 The projected band diagram of the PhC with square lattice of rods. Orange line indicates the allowed modes introduced to the band gap by the linear defect, and the black line indicates the allowed frequency of the resonance cavity. 35
Figure 3.3 **(a)** Schematic of the simulated two-dimensional rod-type PhC after the insertion of the Fano rod. **(b)** The transmission spectrum of the device that is shown in **(a)**. 37
Figure 3.4 The transmission spectrums of Lorentzian Configuration and Fano-like configuration. **(a)** Logarithmic scale. **(b)** Linear scale. 38
Figure 3.5 **(a)** Transmission spectrum when different gases are introduced in the simulation environment, from left to right: Air, Acetylene Chlorine and SF_6. **(b)** Plot of wavelength shift per change in the background refractive index. The sensitivity value is found as 1039 nm/RIU. 41
Figure 3.6 Variation of Q-factor with respect to background index shift..... 42
Figure 3.7 FDTD analysis of the structure **(a)** Ez mode profile of the fundamental resonance of the cavity. **(b)** Normalized Electric Field (Ez) Slice of the cavity area. 43
Figure 3.8 Mesh structure of a 2D PhC via COMSOL..... 45
Figure 3.9. 3D CAD drawing of the structure. **(a)** Isometric view **(b)** Cross-sectional view. 48
Figure 3.10. **(a)** Cavity Resonance Electric field profile when an air gap of 50 nm is inserted. **(b)** Electric field slice from the center of the cavity along the x-axis. 49

Figure 3.11 Transmission spectrum of the device after replacing PEC plates with Gold plates with varying background indices. Q-factor is calculated as 487. The black line represents the background as air and the red line represent a 0.001 shift in the background refractive index. 51
Figure 3.12. The transmission spectra of the device for varying gap sizes and background refractive indices. The simulation environment where the background is air is plotted with solid lines and the dashed lines represent the background index shift of 10^{-3} RIU. 52
Figure 3.13 Illustration of the device as parallel plate capacitance for resonance tuning. 54
Figure 4.1. Illustration of interference patterns. The solid light blue line and dashed green line represent the two waves that undergo interference and the solid black line represents the resultant wave. **(a)** Destructive Interference **(b)** Constructive Interference. 58
Figure 4.2 The band diagram for the 2D hexagonal lattice for band transition. The dashed blue line represents the off-state and the solid blue line represents the on-state. 60
Figure 4.3 Observation of negative refractive index from mode profile. **(a)** Positive refraction. **(b)** Negative refraction. [52] 60
Figure 4.4. **(a)** Field intensity of the input signal for both arms. **(b)** The PhC structure and mode profile for the Control side and Device side. **(c)** The field intensities at the output side of both signals.[52] 61
Figure 4.5. Mode profile of 2D PhC MZI. **(a)** Non excited state (off-state) **(b)** Excited state (on-state) 62
Figure 4.6. Schematic of the simplified version of the experimental setup 64
Figure 4.7. Experimental setup. 65
Figure 4.8. Zoomed out SEM Image of the fabricated chip 66
Figure 4.9. **(a)** The layout of the designed PhC structure. **(b)** SEM image of PhC part of the MZI. 67
Figure 4.10.**(a),(b),(c),(d)** SEM image of various sized PhC structures. 68

Figure 4.11. Transmission spectrum from PhC structure with r=160 nm. The blue line represents the short PhC structure (which has less number of unit cells in the direction of the propagation), the orange line represents the longer PhC where band gap is clearly seen around 1550 nm wavelength. 69
Figure 4.12. Intensity modulation of the MZI with optical carrier injection. 70

LIST OF ABBREVIATIONS

ABBREVIATIONS

CMOS:	Complementary Metal Oxide Semiconductor
FDTD:	Finite Difference Time Domain
FEM:	Finite Element Method
MEEP:	MIT Electromagnetic Equation Propagation
MPB:	MIT Photonics Bands
PhC:	Photonic Crystal
RIU:	Refractive Index Unit
SOI:	Silicon-On-Insulator
SRP:	Surface Plasmon Resonance
TE:	Transverse Electric
TIR:	Total Internal Reflection
TM:	Transverse Magnetic
WGM:	Whispering Gallery Mode

LIST OF SYMBOLS

SYMBOLS

a:	Lattice Constant
B:	Magnetic Flux Density Vector
D:	Electric Displacement Vector
E:	Electric Field Intensity Vector
H:	Magnetic Field Intensity Vector
J:	Current Density Vector
k:	Optical Wave Vector
n_{eff}:	Effective Refrective Index
Q:	Quality Factor
S:	Sensitivity
Si:	Silicon
SiO_2:	Silicon Dioxide
SF_6:	Sulfur Hexafloride
ϵ:	Dielectric Permittivity
ϵ_r:	Relative Dielectric Permittivity
μ:	Magnetic Permeability
ω:	Optical Angular Frequency
ρ:	Volume Charge Density

CHAPTER 1

INTRODUCTION

Manipulating light propagation is one of the most active research areas for both scientists and engineers and fascinating new studies have been conducted through the last decades [1]–[7]. Some of the most impactful studies have proven that that the concept of 'semiconductor' for electrons can be created for photons inside a transparent (lossless) dielectric medium. The periodical arrangement of alternating dielectric media, which is called a Photonic Crystal (PhC), enables creating photonic bands for photons, a well-known phenomenon which is the energy bands for electrons inside a semiconductor [4]. Photonic Crystals can be made with many different types of materials; however, the focus of this thesis is on Silicon PhCs. With the advancements in silicon processing technology and PhCs are being highly customizable, the device characteristics are extremely configurable so very distinct and robust devices can be fabricated [5]–[12]. The periodical arrangement of alternating dielectric media is constructed with the smallest building blocks called unit cells. The shape, lattice configuration and dielectric contrast of the unit cell creates a spectral region called a photonic band gap where the light with a frequency that resides in this region is not allowed to propagate. Using this region, a trap state can be created by perturbing a number of unit cells, like introducing an intentional defect called an optical cavity that allows the presence of light inside with frequencies residing in the band gap. If, somehow, the light couples to that region, it is both spatially and temporally confined since it has nowhere to go due to the presence of band gap. This allows an immense amount of applications possible such as optical modulators, switches, accelerometers, detectors and bio-sensors as well as some very interesting physical phenomena like slow-light effect, zero-n materials, light trapping and optical memory systems [3], [13]–[28].

1.1 Gas and Bio-Sensing

Bio-sensing applications area is one of the domains that can considerably benefit from switching from electrical-based to optical-based. In many sectors, such as medicine and military-based applications, detection and differentiation of harmful microorganisms, proteins, DNA, malignant cells, and various types of gases and airborne chemicals are crucial for accurate diagnosis, sensing systems, and gas-leak detection [22], [23], [29], [30].

Because of several obvious advantages such as small footprint, extremely high sensitivity, stability, and immunity to electromagnetic interference, extensive research has been conducted in the field of bio-sensing applications using an optical approach. [31]. To detect the change in the refractive index of the analyte is one of the most widely used methods of optical sensing [29], [30], [32], [33]. One main advantage of refractive index sensing is label-free sensing is possible with this way where the sensing operation does not require any special interface material to interact with the target analyte for detection. The presence of the analyte in these devices alters the background refractive index or causes local index perturbations. The intensity and/or the phase of the transmitted output wave changes as the refractive index changes. There are many different device configurations that utilize this way of sensing such as ring resonators, surface plasmon resonance (SPR) devices, whispering gallery mode (WGM) and PhC cavities [34]–[43]. PhC cavities, with their highly customizable device characteristics, low-loss transmission properties, small foot-print, complementary metal oxide semiconductor (CMOS) compatibility and integration advantages step forward among other methods [44], [45].

1.2 All Optical Switching and Modulation

Optical communication systems have become beyond doubt one of the most important technological fields in our era since vastly increasing data rate, and the increasing physical distance of the two communicating devices. This forced

scientists and engineers to transition from electrical communication to optical communication with the development of fiber-optical cables and ultra-high bandwidth and wavelength division multiplexing (WDM) properties of waveguides that allow transmission of multiple signals in the same medium [46], [47].

The main parts of an optical communication system can be described as follows; the light source to generate light as the carrier, fiber optic cables for transmission medium, modulators for load the light with the actual information that will be sent to the output, and an optical receiver for reading the transmitted data at the output. The modulation process is critical since the actual message is loaded to the carrier signal. The preferred modulation method is the digital modulation where binary information is used with high and low intensity corresponds to on and off state, in other words, “1” and “0” bits. This is called intensity modulation and it is a simpler method since the photodetector directly receives the exact bits of the signal.

The optical data transfer was first available on a larger scale such as fiber-to-device and with the improvements on the fabrication technology it shrunk down to device-to-device, chip-to-chip. In the past years, optical communication systems are started to appear on chip scale integrated circuits [47], [48]. The development and maturity of the CMOS fabrication process allowed CMOS compatible integrated photonic circuits. As it was stated before, PhC structures and their band gaps can be altered to have many interesting design types and one of the application area is the Silicon PhC optical modulators since they are both CMOS compatible, offer an extremely small footprint, high operation speed and low power consumption [4].

An optical modulator mainly controls the output signal based on several properties of the light listed as; amplitude, phase and polarization. Those properties can be altered by changing the refractive index of the material via several ways such as Kerr’s effect where the refractive index of the medium is changed under the applied electric field along the direction of propagation, making the medium birefringent. This effects is observed strongly in some amorphous materials and change of the refractive index is quadratically proportional to the magnitude of the applied E-field

[49]. Pockel's effect is also similar to Kerr's effect which alters the refractive index of the medium by applying E-field. It has a lower effect than Kerr's effect and the relation of the applied E-field magnitude and change in the refractive index is linear [50]. Another important effect is the Franz-Keldysh Effect, where the energy band diagram of a III-V semiconductor is modified under the applied E-field and photon absorption occurs, even for the photons with the energy that is lower than the band gap of that semiconductor [51]. The reason for that is the wave functions of the valence band and conduction band starts to partially overlap with the increasing E-field and a tunneling phenomenon is starting to be observed [51].

The abovementioned effects apply relatively small changes in the refractive index. The aim is to reduce the required power, increase the speed and bandwidth, and shrink the device sizes when it comes to optical modulation. So another effect is investigated and experimentally used in this work, which is the Plasma Dispersion Effect. The refractive index shift of the medium is directly proportional to the number of electron and hole carriers inside the medium. This effect is widely used especially for Silicon based devices since a high enough refractive index shift is possible with the plasma dispersion effect on Silicon [51]. The change in the refractive index of bulk Silicon is formulated as in Equation 1.1 for 1550 nm wavelength [51]

$$\Delta n = \Delta n_e + \Delta n_h = \{-8.8x10^{-22}x(\Delta N_e)\} + \{-8.5x10^{-18}x(\Delta N_h)^{0.8}\} \quad (1.1)$$

where Δn_e, Δn_h, are the change of the refractive index due to electrons and holes, ΔN_e, and ΔN_h, are the change in the electron and hole concentrations respectively. The carrier density can be increased in several ways: a p-n, a p-i-n diode structure, a MOS structure, or optical carrier injection [52].

1.3 The Scope of the Thesis

This thesis has two main works both are concentrated around Silicon PhC bandgap applications. The first one is an optical Gas/Bio-sensor structure that has ultra-high

sensitivity with high tunability characteristics. Out-of-plane light confinement is achieved using reflection in the suggested structure, which comprises 2D PhC silicon rods sandwiched in the perfect electric conductor (PEC) plates. Sharp asymmetric Fano-like resonance boosts the Q-factor, making it ideal for sensing applications. A small air gap between the top of the silicon rods and the metallic plate is used to create the tuning mechanism. This air-gap functions as a slot structure, confining E-Field to a narrow area while simultaneously boosting sensitivity and reducing mode volume. The gap size can be changed via electrostatic actuation by applying a voltage difference between the PEC plates, which will be replaced with Gold plates for fabrication. The second application is the experimental confirmation of an optical MZI modulator by optical excitation. The structure is built on 260 nm thick SOI wafer on top of 2 μm deep buried oxide layer. The patterns were fabricated by E-beam lithography and RIE etching. By exploiting and carefully engineering the PhC band diagram, a band to band transition occurs and negative phase accumulation is achieved. This significantly increases the effective refractive index change of the mode ~-4, while changing the bulk silicon index by 0.01. By optical carrier injection method with a 100 mW power, and an operation wavelength of 520 nm laser, the modulation is experimentally confirmed.

1.4 Organization of the Thesis and Thesis Contribution

The organization of the thesis is composed of 4 Chapters. In Chapter 2, the theoretical background regarding electromagnetic waves and photonic crystal is briefly investigated. The analysis starts with the fundamental Maxwell's Equations and then continues with the light propagation in the periodic media. Then, photonic crystals and photonic band gap is analyzed and the reader is informed with common PhC structures and cavities. In Chapter 3, the design procedure of the optical bio-sensor is analyzed in detail. The design steps, figures of merit and sensitivity analyzes were performed. Then, the tuning mechanism and the effects of Gold plates are investigated and the results are presented. Chapter 4 covers the second part of the

thesis which is a MZI based optical modulator. The chapter starts with a brief explanation of the experimental setup, commonly used devices and their configuration during the experiments is presented. Then, brief introduction and working principles of MZI are presented. The scanning electron microscope (SEM) images of the devices and their designed layout sizes are compared. After that, the measured results are presented in both transmission spectra and the oscilloscope images. Finally, the Chapter 5 concludes and elaborates on the work done in this thesis and explains what the plans for future studies are.

There are one journal and one conference presentation publications based on the gas/bio-sensor application [18][53]. The project which was funded by TUBITAK is finalized and the final report was presented to TUBITAK. Also, the modulator data and other results are being processed and will be submitted as a journal paper.

CHAPTER 2

BACKGROUND INFORMATION

This chapter is dedicated to help the reader understand the basic concepts that this study is built upon. After a brief explanation of Maxwell's Equations and basic Electromagnetic Theory concepts, the basic principles of more sophisticated and niche concepts of PhCs and electro-static actuation are presented.

2.1 Electromagnetics Background

Electromagnetics is a branch of physics that studies the electromagnetic wave behavior in a medium and the physical interactions between the charged particles. The light, which is an electromagnetic wave, that the human eye can see resides in a tiny region in the electromagnetic wave spectrum as shown in Figure 2.1. It is crucial to know the fundamental concepts of electromagnetics to use and exploit the properties of light. The readers should be able to understand the basics concepts of electromagnetics with the help of the information provided here.

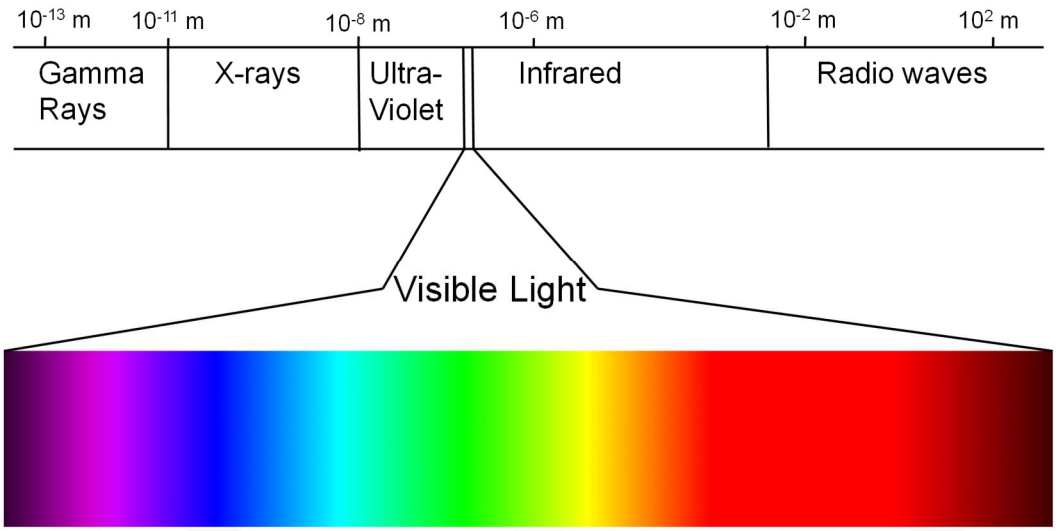

Figure 2.1. The electromagnetic wave spectrum

2.1.1 Maxwell's Equations and Wave Equation

James C. Maxwell unified the Electrical Field and Magnetic Field equations and derived a couple of equations known as Maxwell's Equations. These equations are the building block of any application that uses Electromagnetic waves along with the Wave equations which will be described later. The Macroscopic Maxwell's Equations in the differential form are given in the following equations 2.1, 2.2, 2.3 and 2.4 [4].

$$\nabla . \boldsymbol{D} = \rho \tag{2.1}$$

$$\nabla . \boldsymbol{B} = 0 \tag{2.2}$$

$$\nabla \boldsymbol{x} \boldsymbol{E} + \frac{\partial \boldsymbol{B}}{\partial t} = 0 \tag{2.3}$$

$$\boldsymbol{\nabla x H} - \frac{\partial \boldsymbol{D}}{\partial t} = \boldsymbol{J} \tag{2.4}$$

The symbols $\boldsymbol{D}$ and $\boldsymbol{B}$ represent electric displacement vector and magnetic flux density and also, $\boldsymbol{E}$ and $\boldsymbol{H}$ represent the electric field and magnetic field respectively. $\boldsymbol{J}$ is the current density and ρ is the charge density.

Maxwell's Equations can be simplified for a source-free and non-magnetic medium. To make things easier, the medium can be assumed to be linear and isotropic where the dielectric permittivity (ϵ) and the magnetic permeability (μ) are also independent of the field amplitudes. Throughout this study, the materials of interest will be mostly Si and SiO_2 where Au will take place for the final parts. The materials and the frequency of the operation which resides in the near-infrared range enable the previous assumptions. Thus, $\boldsymbol{J}$ and ρ are removed from the original Maxwell' Equations. By utilizing the above-mentioned points and the Maxwell's Equations, the wave equation can be driven. The wave equation is the main equation that is being used for the analysis of electromagnetic waves in a medium. The derivation of the wave equation can be started with the curl operation of Equation 2.4 to obtain Equation 2.5.

$$\nabla \mathrm{x}\left(\nabla \boldsymbol{x}\boldsymbol{H} - \frac{\partial \boldsymbol{D}}{\partial t}\right) = 0 \tag{2.5}$$

The electric displacement vector $\boldsymbol{D}$ can be replaced by $\epsilon\boldsymbol{E}$. Keeping in mind that ϵ is independent of time and position, so it is treated as a constant. Using the same principles, $\boldsymbol{H}$ is also replaced with $\boldsymbol{B}/\mu$ and Equation 2.6 is obtained after the mentioned operations.

$$\nabla \mathrm{x}(\nabla x\boldsymbol{B}) - \mu\epsilon \frac{\partial}{\partial t}(\nabla x\boldsymbol{E}) = 0 \tag{2.6}$$

Now Equation 2.3 is substituted into Equation 2.6 and Equation 2.7 is obtained.

$$\nabla \mathrm{x}(\nabla x\boldsymbol{B}) = -\mu\epsilon \frac{\partial}{\partial t}\left(\frac{\partial \boldsymbol{B}}{\partial t}\right) \tag{2.7}$$

Equation 2.7 presents a decoupled equation with $\boldsymbol{B}$ as the only variable. Further simplifications can be made to get rid of the curl operation using the vector identity in Equation 2.8.

$$\nabla \mathrm{x}(\nabla x\boldsymbol{B}) = \nabla(\nabla.\boldsymbol{B}) - \nabla^2.\boldsymbol{B} \tag{2.8}$$

From Equation 2.2 the first term of the right hand side cancels out and the final form of the wave equation is obtained in Equation 2.9. The same equation can be driven for the Electric Field given as the variable and it is also given in Equation 2.10 [54].

$$\nabla^2 . \boldsymbol{B} - \mu\epsilon \frac{\partial}{\partial t}\left(\frac{\partial \boldsymbol{B}}{\partial t}\right) = 0 \tag{2.9}$$

$$\nabla^2 . \boldsymbol{E} - \mu\epsilon \frac{\partial}{\partial t}\left(\frac{\partial \boldsymbol{E}}{\partial t}\right) = 0 \tag{2.10}$$

2.1.2 Propagation of Light in Periodic Media and Photonic Crystals

A photonic crystal (PhC) is a metamaterial with periodically alternating dielectric constants in a certain direction. This spatial variation of periodic dielectric constants creates a uniform structure, which results in a crystal structure. This vector of periodicity can be in 1, 2 or 3 dimensions. An illustration of photonic crystals is shown in Figure 2.2.

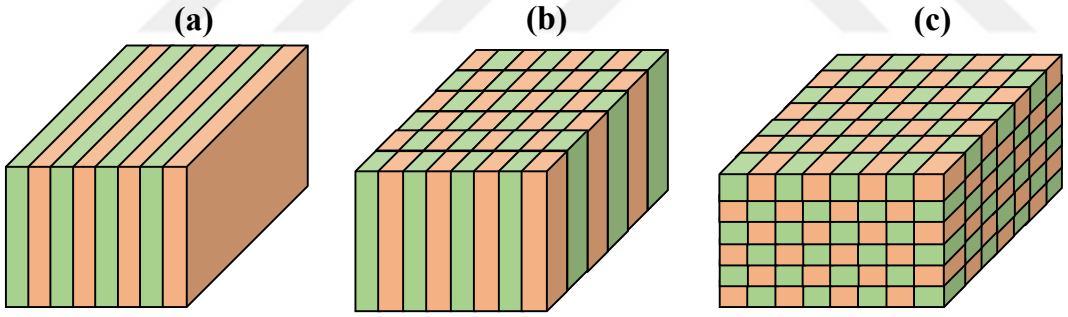

Figure 2.2. Representation of Photonic Crystals. **(a)**, **(b)**, **(c)** are one dimensional, two dimensional and three dimensional respectively. Differing colors means different medium with varying dielectric constants.

Early studies on PhCs were conducted by Yablonovitch [55] and Sajeev John [56] and it made a significant impact on optics-photonics research. To understand the PhC concept, one can use the analogy between PhC and semiconductor crystals. Due to its periodicity, PhCs have a band gap, which is a spectral region, where the light with such frequencies is not allowed to propagate, just like a semiconductor crystal's band gap, where an electron is not allowed to have the energy levels which reside in the

band gap. One major advantage of PhCs is that the band diagram can be engineered to have the desired characteristics, by manipulating physical properties (dimensions, shapes, periodicity, materials, etc.). The unit cell is the building block of any PhC and the physical properties of a unit cell define the whole device characteristics. An illustration of a unit cell for a PhC slab with an air hole on it is given in Figure 2.3. The main and the most important parameters are the lattice periodicity (*a*), slab thickness (*h*), hole radius (*r*) and the materials' dielectric constants.

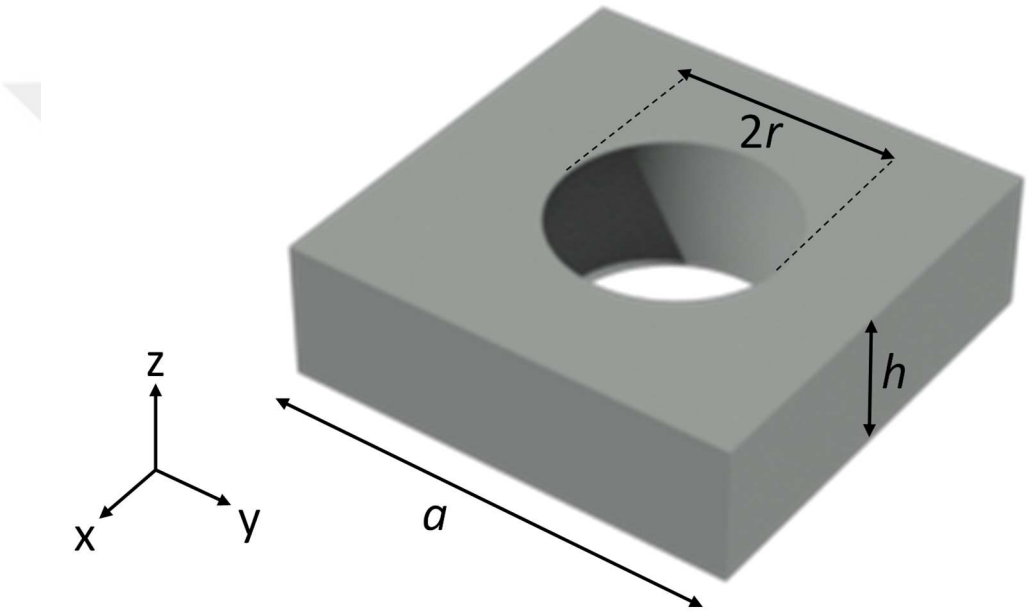

Figure 2.3. Representation of a unit cell for a PhC. The parameters are listed as; *a* is the lattice constant, *r* is the hole radius and *h* is the slab thickness.

The crystal lattice structure is also another important parameter of the device characteristics; two of the most common lattice structures are square lattice and hexagonal lattice. As their name implies, it defines the periodicity of the vector. In Figure 2.4(a), a scanning electron microscope (SEM) image of one of our own fabricated PhC structures with hexagonal lattice is shown. In Figure 2.4(b), the cross sectional view of a similar PhC unit cell is shown.

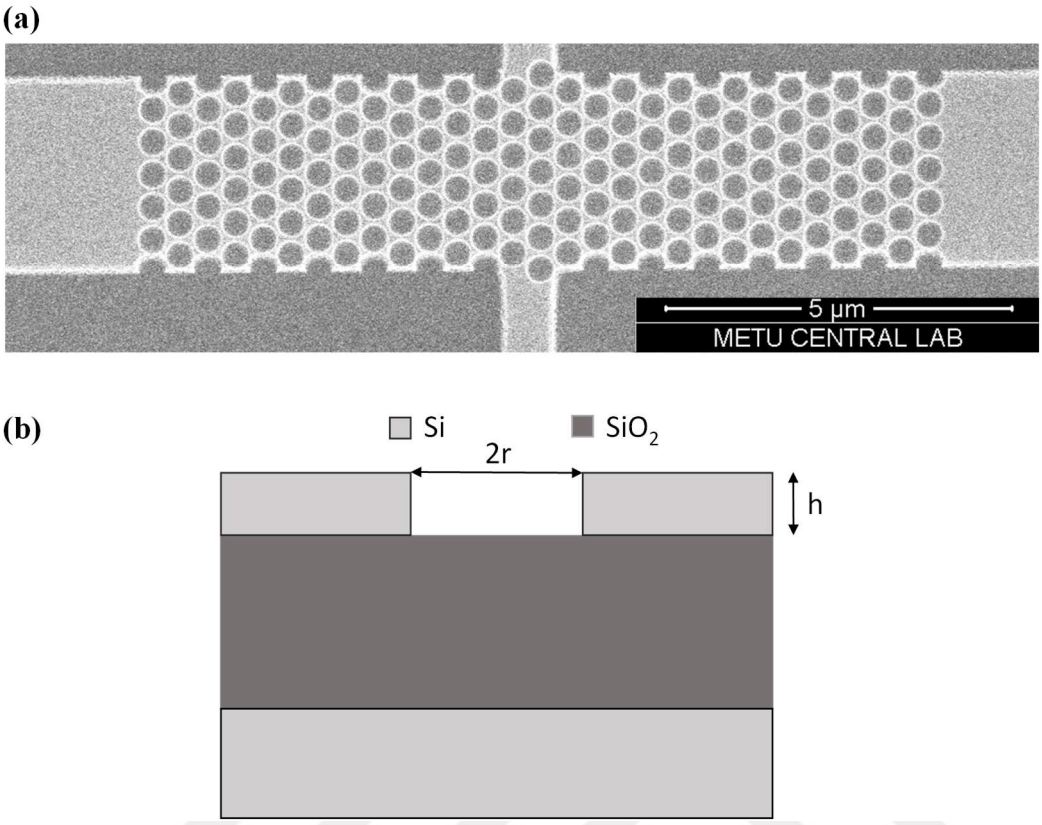

Figure 2.4. **(a)** SEM image of a PhC with hexagonal lattice structure in the middle of a waveguide. 220 nm Silicon wafer on 2 µm buried oxide layer patterned with Electron-beam lithography. Lattice constant and hole radius are 460 nm and 360 nm respectively. **(b)** Cross Sectional view of a unit cell.

For simplicity, a PhC with a square lattice with dielectric rods will be analyzed and its band diagram will be obtained in the next part. To find the mods which are allowed to propagate in a PhC, the wave equation must be solved. However, it is important to take advantage of the periodicity of the PhC. Since PhCs are periodic and uniform structures, the concept of the reciprocal lattice can be applied [4]. The reciprocal lattice is the analysis of spatial lattice in the frequency domain. This concept of reciprocal lattice combined with Fourier transform allows straightforward analysis of the interaction of waves with periodic structures. The electromagnetic modes of any structure with translational symmetry, like PhCs, can be classified by the wave vector $\boldsymbol{k}$. For a plane wave with magnetic field $\mathbf{H}(r)=\mathbf{H}\exp(ik\cdot r)$, the eigen values for this equation can be obtained after solving Equation 2.11.

$$\nabla x \left(\frac{1}{\epsilon_r(\boldsymbol{r})} \nabla x \boldsymbol{H}(\boldsymbol{r}) \right) = \left(\frac{\omega}{c} \right)^2 \mathbf{H}(\boldsymbol{r}) \tag{2.11}$$

where ϵ_r ,$\boldsymbol{r}$, ω and c are the spatial relative permittivity, the position vector, angular frequency and the speed of light in vacuum and also, the eigenvalue is $(\omega/c)^2$. The in-depth analysis of a PhC can be conducted via obtaining and inspecting the band diagram.

2.1.3 Photonic Band Gaps

The photonic band gap as stated before, is the spectral region where the light is not allowed to propagate inside the medium. This work is built on manipulating the photonic band gaps and get the desired characteristics via fabricating the PhC as desired. One important concept is to understand is the physical origin of photonic band gaps and how they exist. If we consider a medium that is given in Figure 2.2**(a)** and the wave is propagating entirely in the normal incidence of the dielectric sheets. If we assume that the medium is homogenous, the speed of light will be reduced by the refractive index of the medium *n*. So a light line of $\omega(k) = \frac{ck}{n}$ will be created. Since the wave vector *k* is assumed to repeat itself outside of the Brillouin zone (which will be explained in the next part) the light line folds unto itself when reaching an edge of this zone. The photonic band gap appears when the medium is not homogenous and there is a refractive index difference between the two materials. Also, the band gap widens when the dielectric constant contrast is increased.

The existence of band gap is best understood when investigating the E-field profiles of the modes just above (*n* =2) and below (*n* =1) the band gap. To obey the symmetry for the Bloch's Theorem [57], the modes should either concantrate their energy on the low-index region or the high-index region. The modes with lower frequency (near band *n* =1) and higher frequencies (near band *n* =2) tend to concentrate their energy on the high-index region and low-index region respectively. Although it is not always the case, the lower band is called dielectric band and the upper band is

called the air band [4]. An example of this mode confinement is shown in Figure 2.5. The red line shows the intensity of the E-field and dark and light gray area shows the high index and low index medium respectively.

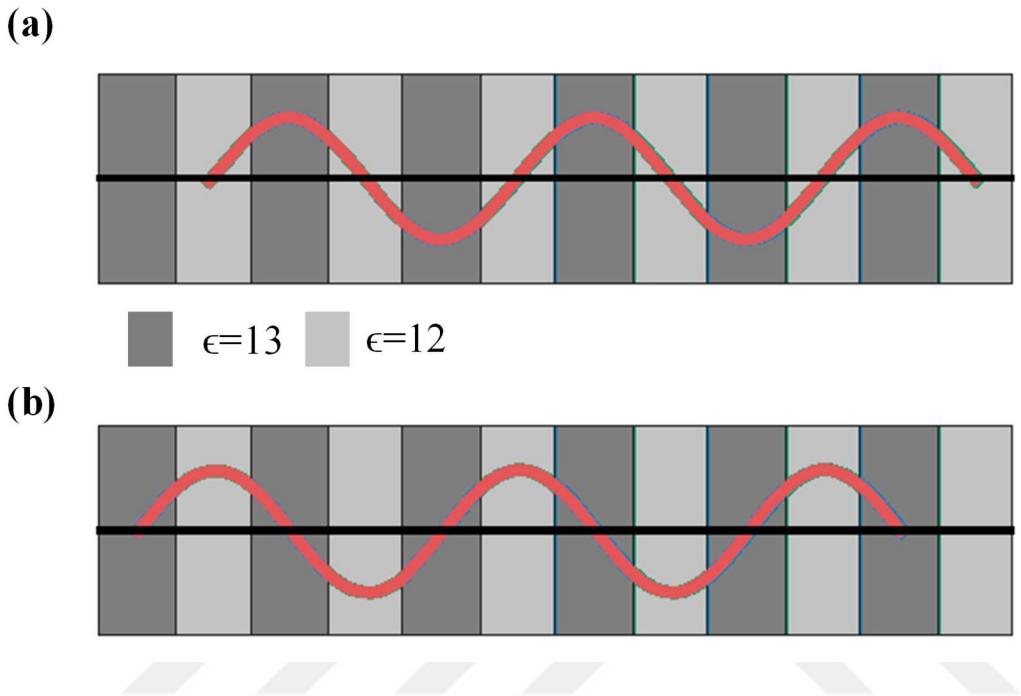

Figure 2.5 Electric field confinement on periodic media with dielectric constants of 13 and 12. **(a)** The mode profile of the dielectric band mode **(b)** The mode profile of the air band mode

Since both modes are just below and top of the band gap, it is intuitive that they should have different frequencies, and as the dielectric constant increases, the frequency difference also increases, which results in a wider photonic band gap [4].

2.2 Analysis of Photonic Crystals

According to the dimensions of their periodicity, PhCs can be classified into three groups which are, one-dimensional PhC, two-dimensional PhC and three-dimensional PhC. Independent of the direction of the periodicity, the conventional way to design a PhC starts with extracting its band diagram. Band diagram contains the dispersion relation inside the crystal, usually, the vertical axis corresponds to the

normalized optical frequency and the horizontal axis being the ***k***-space. By looking at a band diagram, many properties of the device can be obtained such as, what will be the effective refractive index for a given frequency, which modes will be supported, where will the no-transmission zone will be, etc. Such calculations were done with MIT-Photonic-Bands (MPB) software package in this thesis [58].

The main numerical methods that have been utilized are the finite-difference time domain (FDTD) method and finite element method (FEM). FDTD method is a highly used method for many studies that require the investigation of electromagnetic waves, especially nano-scale optical devices and PhCs. The method discretizes the Maxwell's equations for both space and time on a mesh for the given simulation medium and computes **E** and **H** fields for each grid point. It is a powerful tool that incorporates transmission, absorption, reflection and scattering analyses. Since it gives a time-domain solution, the wave behavior can be observed inside the simulation environment, especially useful for observing optical switches and resonator structures. Many of the field distributions and transmission spectra in this thesis obtained by MEEP software package [59].

Another important numerical method is the finite element method (FEM). It is a widely used method for solving differential equations in all kinds of engineering fields. The main principle of FEM is to divide a bigger system into many smaller subsystems called finite elements. It is achieved by spatially dividing the system into meshes, and solve the partial differential equations for each boundary condition. For this thesis, it doesn't provide a time based solution like FDTD. However, it is used for plasmonic effects such as absorption and reflection for metal surfaces. The FEM software is selected as COMSOL Multiphysics [60].

2.2.1 One-dimensional PhCs

Probably, the simplest of the PhCs is the one-dimensional PhCs. Their structure has discrete translational symmetry in one direction and consists of alternating materials

only along one direction. Using the unit cell shown in Figure 2.3 a one-dimensional PhC can be constructed by periodically arranging the unit cell and results in a structure called PhC nano-beam, shown in Figure 2.6(a) and Figure 2.6(b). The dispersion relation for a transverse-electric (TE) polarized light is extracted by using MPB. The result of this extraction is given in Figure 2.6(c). The Bloch modes allow the light guiding in the direction of propagation and the light is confined in the device by total internal reflection (TIR) [57].

As it can be seen from Figure 2.6(c), there are two bands named Band 1 and Band 2. They represent the allowed frequencies for the light propagation. Each frequency on those bands will be guided with its corresponding wave vector $\boldsymbol{k}$. There are also two regions of importance. One is the band gap region, the light with the frequency that resides in this region is not allowed to propagate. It is analogous to the energy states for electrons in a crystal material. It is a crucial aspect of all PhCs since it can be engineered as much as the physical limitations allow. The *k*-space is the definitive factor to find the dispersion relation for a given input light with the frequency. Here for one-dimensional PhC, the position of any unit cell can be defined as in Equation 2.12.

$$\boldsymbol{R} = m\boldsymbol{a}\boldsymbol{x} \tag{2.12}$$

where $\boldsymbol{R}$ is the lattice vector, m is an integer, a is the lattice periodicity and $\boldsymbol{x}$ is the unit vector along the x-direction shown in Figure 2.6(a). By using the periodicity in *k*-space, the reciprocal lattice vector $\boldsymbol{b}$ can be written as in Equation 2.13 [4].

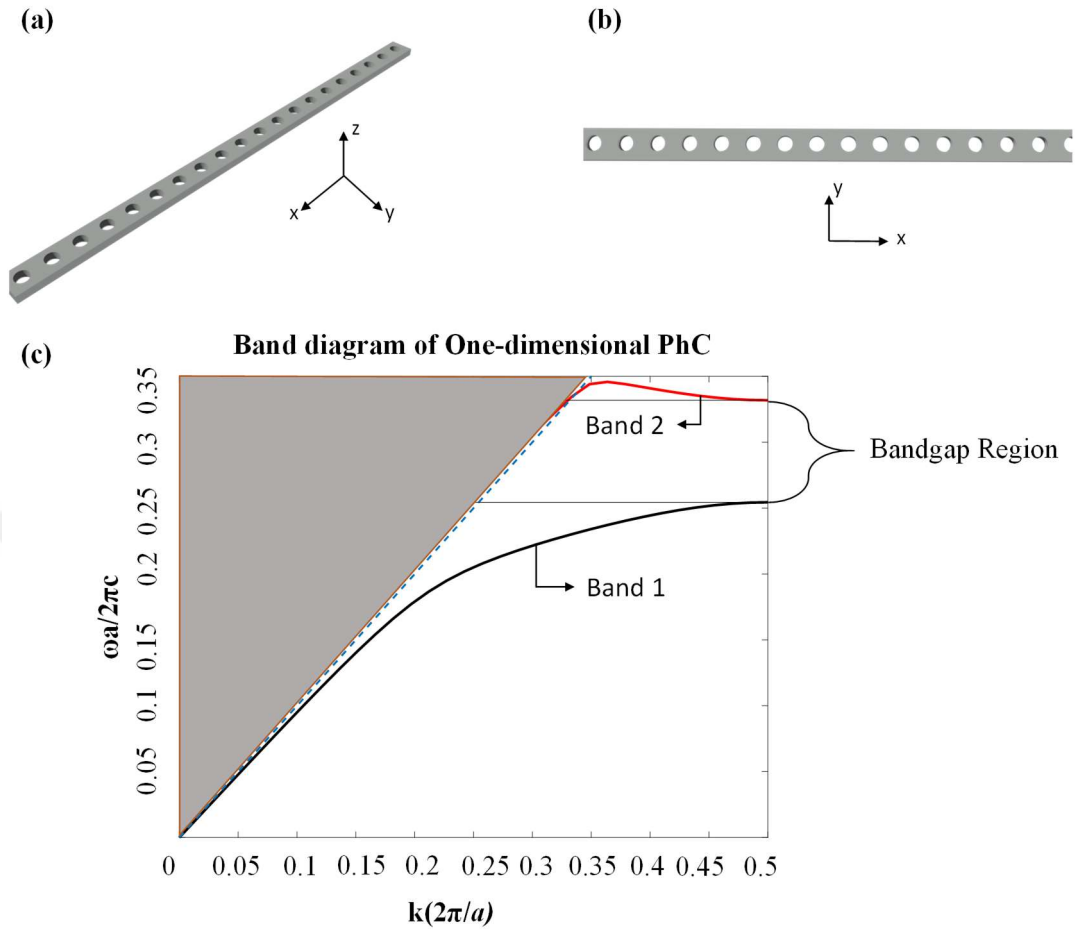

Figure 2.6. **(a),(b)** Illustration of one-dimensional PhC. **(a)** Isometric view. **(b)** Top view. **(c)** Band diagram of one-dimensional PhC.

$$\boldsymbol{b} = \mathrm{m}\frac{2\pi}{a}\boldsymbol{x} \tag{2.13}$$

In this part *k*-space is contained only in one direction which is x-direction. A detailed analysis of Brillouin-zone and *k*-space will be given for the two-dimensional PhC in the next part.

Another important region on Figure 2.6(b) is the gray area on the left side of the band diagram. For a PhC nanobeam, the light is contained in the device via TIR and the method of guiding is called index guiding. So, it is the primary condition to be satisfied for any device that utilizes index guiding. Hence, the effective refractive index of the mode for a light to be guided in the transverse direction must be larger

than the refractive index of the cladding material. In the previous example, the cladding is air both on top and bottom of the PhC nanobeam so it is taken as one. For asymmetrical structures, however, the larger refractive index for the cladding is chosen. Here, the region where the light is not guided is called the light cone, and the line separating the band diagram to two, the light line. The light cone is shown as a gray area in Figure 2.6(b). The light in this region is coupled to the radiation modes and dissipate through the air.

Many different types of devices were fabricated and published using one-dimensional PhC nano-beam devices such as modulators, sensors, detectors etc [61]–[63].

2.2.2 Two-dimensional PhCs

Two-dimensional PhCs are generally more common in the literature. The difference is that they have two vectors for periodicity, one for the x-direction and another for the y-direction based on the selected planes. An example of a fabricated two-dimensional PhC is already given in Figure 2.4(a). One of the most common lattice configurations is square lattice and hexagonal lattice for two-dimensional PhCs. In Figure 2.6(a) an example of a two-dimensional PhC of rods with infinite height is given. As can be seen from the figure, it has a periodical arrangement of a square lattice configuration.

The difference is that since there are two symmetry axes, the lattice vector can be written as a linear combination of two unit vectors as given in Equation 2.14.

$$\boldsymbol{R} = ma_x\boldsymbol{x} + na_y\boldsymbol{y} \tag{2.14}$$

where m and n are integers and a_x and a_y are the lattice periodicity along the x and y axes. Similarly to the one-dimensional PhCs, the reciprocal lattice vector can be obtained as given in Equation 2.15.

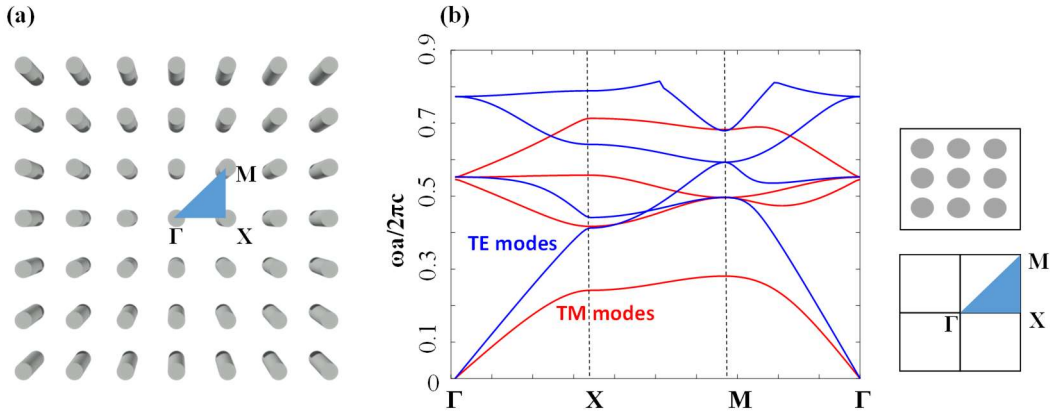

Figure 2.7. **(a)** Illustration of two-dimensional PhC. **(b)** Band diagram of two-dimensional PhC. Blue bands are for TE modes and red bands are for TM modes.

$$\boldsymbol{b} = \mathrm{m}\frac{2\pi}{a_x}\boldsymbol{x} + n\frac{2\pi}{a_y}\boldsymbol{y} \tag{2.15}$$

Taking advantage of the two symmetry axes, analyzing only the region that is indicated by the blue triangle in Figure 2.7(a) gives all of the entire information about *k*-space. This region has a unique name that is the irreducible Brillouin zone [4]. It is a critical concept for investigating all types of periodically arranged structures i.e. the materials with crystal form. The band diagram that is given in Figure 2.7(a) is created with a square lattice of rods with a_x=a_y=a radius of the rods are 0.2a with a dielectric constant ϵ=12. TE and TM band structures are equally important so both of them are shown here. Note that the frequency is normalized with a ratio of $\omega a/2\pi c$. Here the horizontal axis represents the direction of in-plane wave vector from Γ to X to M to Γ again which is the edges of the blue triangle that represents the irreducible Brillouin zone. At first glance, it seems like a complicated diagram, but with further investigation, it becomes clear that the minima and maxima of a band gap commonly occur at the edges of the Brillouin zone. Although the PhCs are highly customizable and there are many examples, there are some rules of thumbs such as, the TM gap favors the square lattice configuration with dielectric rods, and the TE gap favors the hexagonal lattice configuration of air holes inside a dielectric slab. By comparing Figure 2.6(c) and Figure 2.7(b) it is clearly seen that the former has a gap

for the TE polarized light and the latter exhibits a large band gap for a TM polarized light. For two-dimensional PhC slab structures, TE-modes and TM-modes are sometimes referred to as even modes and odd modes. The modes are characterized by the spatial E-field profile to the slab plane. A mode is categorized as “even” when the majority of the E-field is confined within the plane of the slab, and for the “odd” modes, the majority of the E-field is confined within the direction that is normal to the slab.

Design parameters such as lattice constant, rod radius, and slab thickness can be manipulated so that the desired band diagram can be obtained. This work utilizes the square lattice of dielectric rods as the PhC for the operation which can be seen as an unorthodox way of utilizing PhCs since many applications are based on etching holes on Silicon with an SOI wafer.

The effect of the dielectric constant is similar to the rod radius. For a given unit cell, the effective refractive index is the important parameter that determines the frequencies of the band diagram. In Figure 2.7**(b)** the bands shift to upper frequencies when the effective refractive of a given unit cell decreases, which can happen in two possible ways; the first way is if the dielectric constant of the rod material decreases, the second way is if the radius of the rod decreases.

2.2.3 Three-dimensional PhCs

In addition to the periodicity on the x and y-directions, if the structure is also periodic in the z-direction the structure becomes a three-dimensional PhC. There are some fabricated examples of three-dimensional PhCs, however due to the difficulties in manufacturing, they are not as mature as one and two-dimensional counterparts [64], [65].

2.3 Localization of Light in PhCs

One of the most important concepts in PhCs is the ability to localize light both spatially and temporally inside a region. As shown before, PhCs exhibits a band gap where the density of states (the number of allowed modes per frequency) is zero. So, by introducing a perturbation inside the lattice, a localized state in the band gap can be introduced to the band diagram. To get a grasp at the concept of introducing a perturbation, examine Figure 2.8 where a two-dimensional rod-type PhC is illustrated. When the rod with the red color is removed, the center of the removed rod shows reflective crystal just like a mirror, in the x and y directions. This is commonly referred to as a "cavity" and if the cavity has the proper size and properties, the cavity introduces a new supported mode in the band gap, and effectively that mode is trapped in the cavity if the coupling occurs. When a defect mode is able to couple to a different mode, it means that the defect mode is no longer completely localized and it is called a leaky mode or resonance [4].

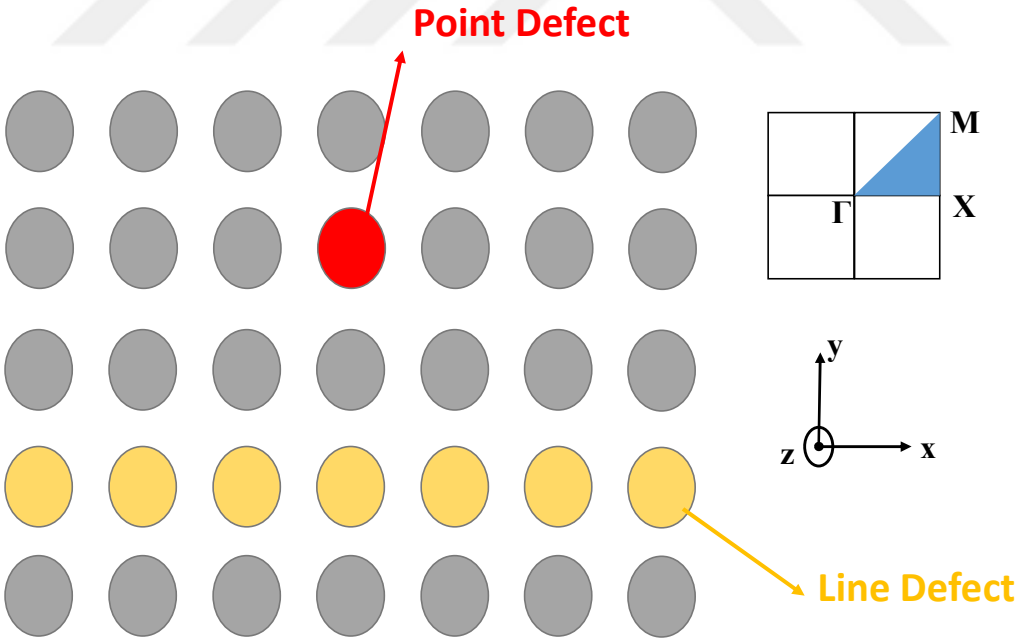

Figure 2.8. Schematic of a Rod-Type two-dimensional PhC from top view. Red cirle indicates the removal of a single rod to create a point defect. Yellow circles indicate the removal of one row of Rods to introduce a line defect.

A resonance mode is not surrounded by a completely reflecting wall, and it will smoothly leak away into the continuum with some rate γ. In practical applications, every PhC has a *finite* number of unit cells, and every defect mode can be considered as resonances and every resonance has some leakage rate γ. The evanescent fields decay into the crystal exponentially, however, the leakage rate can also be decreased by increasing the number of unit cells surrounding the defect. This enables some sort of control over the decay rate, which translates into the Quality Factor (Q-Factor) of the resonance mode.

Aside from the resonances, another commonly used defect type is the linear defects. Linear defects are commonly used as guiding the light between two locations. The concept is to remove a sequence of unit cells, rods for this example given in Figure 2.8, to create a guiding path. The light with the frequency inside the band gap is confined in the y-direction through the reflective walls of the PhC since the discrete translational symmetry is preserved for k_y. For k_x, a new region inside the band gap becomes available, to the light guiding can be achieved in the x-direction. For a mode to be guided without the need of index-guiding like other structures, both frequency component and the wave vector should be properly selected, unlike a point defect, where only a single condition, which is the frequency of the light, should be satisfied to create a resonance. The rule of thumb for choosing the operation frequency is to select the midgap frequency for maximum confinement. Ideally, it is desired that the field vanishes at the boundaries of the waveguide and for the lowest-frequency mode, the width of the waveguide should be designed as one-half of the wavelength. An example of a linear-defect PhC waveguide is given in Figure 2.9.

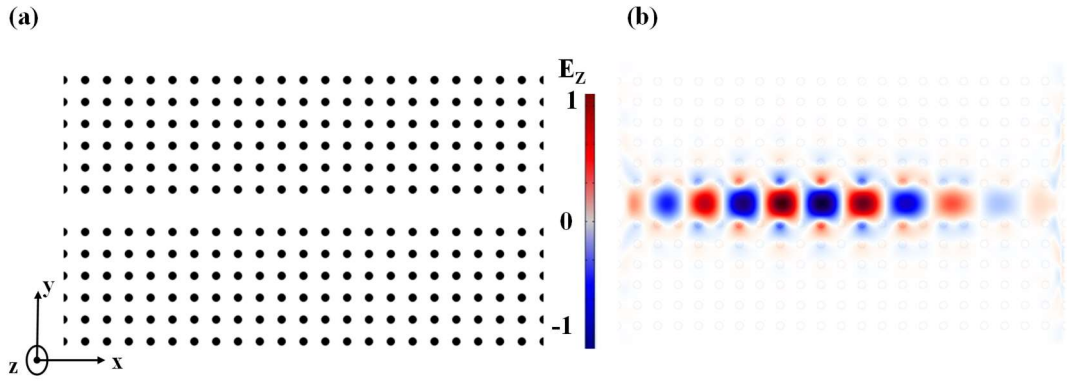

Figure 2.9. Example of a PhC waveguide. **(a)** Top view of the PhC with a linear defect. **(b)** E-field profile with the opertaion wavelength selected as the midgap wavelength. Note that the field is strongly confined in the middle of the PhC waveguide and can't penetrate inside the PhC.

The theoretical foundation of light confinement is based on the temporal coupled-mode theory [66]. It is an important tool that can be used to investigate the light coupling between waveguides and resonators. The theory can be applied to most of the resonators if the Q-factor is sufficiently high. The theory simplifies many parameters and the details of the structure become irrelevant after configuring some of the parameters such as coupling constants, decay factor and resonance frequency. After determining those parameters, many devices can be simplified as a generic resonator.

The temporal coupled-mode theory is developed by using the formalism in [66]. The model that the temporal coupled-mode theory is based on the schematic that is given in Figure 2.10(a).

For this model, the light can go from the input port to the output port by following two possible paths. The first way is the way through coupling to the resonator and then to the waveguide again shown by the black lines, the second way is through the direct path inside the waveguide shown by the gray line in the middle in Figure 2.10(a). The normalized amplitude of the resonance mode is given as a such that the $|a^2|$ corresponds to the energy of the resonance mode inside the cavity, and the time domain equation can be written as Equation 2.16.

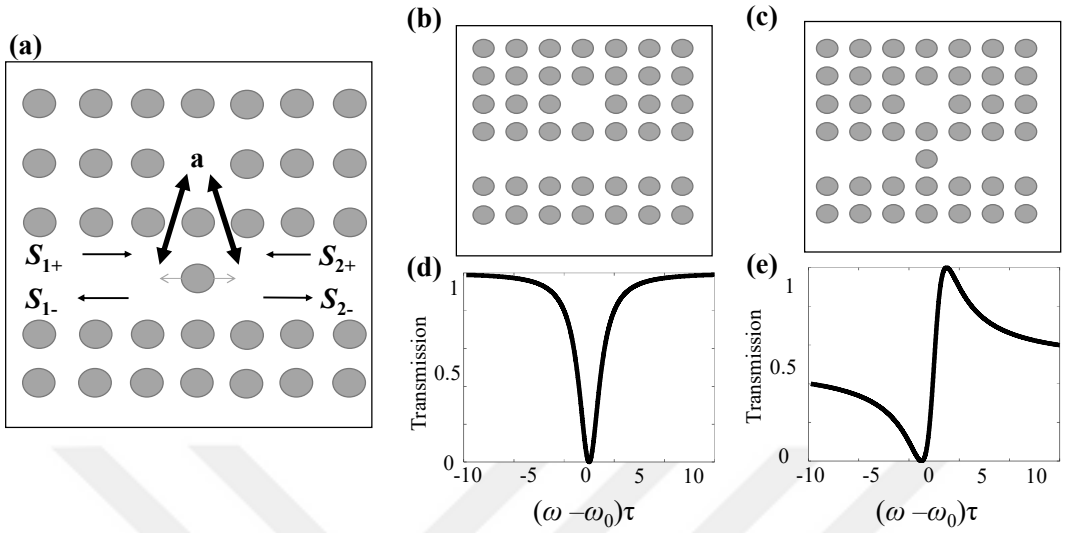

Figure 2.10. Illustration of temporal coupled-mode theory with various structures and generic transmission spectrums. **(a)** Generic resonator model with input and output pathways shown with arrows. **(b)** Schematic of a PhC side coupled cavity. **(c)** Schematic of a PhC side coupled cavity with an additional rod in the middle of the waveguide. **(d), (e)** the generic transmission spectrums for the structures that are provided in **(b)** and **(c)** in order.

$$\frac{da}{dt} = \left(j\omega_0 - \frac{1}{\tau}\right) a + \begin{pmatrix} \kappa_1 & \kappa_2 \end{pmatrix} \begin{pmatrix} S_{1+} \\ S_{2+} \end{pmatrix}, \tag{2.16}$$

$$\begin{pmatrix} S_{1-} \\ S_{2-} \end{pmatrix} = C \begin{pmatrix} S_{1+} \\ S_{2+} \end{pmatrix} + a \begin{pmatrix} d_1 \\ d_2 \end{pmatrix} \tag{2.17}$$

where ω_0 is the resonance frequency, τ is the lifetime of the resonance mode inside the cavity with a Q-factor of $\frac{\omega 0 \tau}{2}$. $\begin{pmatrix} S_{1+} \\ S_{2+} \end{pmatrix}$ are the two input ports to the cavity with the coupling coefficients of $\begin{pmatrix} \kappa_1 & \kappa_2 \end{pmatrix}$. Similarly $\begin{pmatrix} S_{1-} \\ S_{2-} \end{pmatrix}$ are the two output ports with the coupling constants $\begin{pmatrix} d_1 \\ d_2 \end{pmatrix}$. Lastly, *C* is an arbitrary unitary and symmetric matrix that corresponds to a scattering matrix resembling the direct coupling path that is shown with the gray line in Figure 2.10(a). The coefficients κ, *d* and *C* are not

independent and related by energy conversation. The scattering matrix S can be written as,

$$\begin{pmatrix} S_{1-} \\ S_{2-} \end{pmatrix} = S \begin{pmatrix} S_{1+} \\ S_{2+} \end{pmatrix} = \left[C + \frac{1}{j(\omega - \omega_0) + 1/\tau} \mathrm{x} \begin{pmatrix} d_1 \\ d_2 \end{pmatrix} (\kappa_1 \quad \kappa_2) \right] \begin{pmatrix} S_{1+} \\ S_{2+} \end{pmatrix}$$
$$= \left[C + \frac{1}{j(\omega - \omega_0) + 1/\tau} \begin{pmatrix} d_1\kappa_1 & d_1\kappa_2 \\ d_2\kappa_1 & d_2\kappa_2 \end{pmatrix} \right] \begin{pmatrix} S_{1+} \\ S_{2+} \end{pmatrix} \quad (2.18)$$

The amplitude of the resonant mode is also can be written as,

$$a = \frac{1}{j(\omega - \omega_0) + 1/\tau} + (\kappa_1 S_1 + \kappa_2 S_2), \quad (2.19)$$

If we consider the case where no input wave excitation, and only a resonant wave exist in the cavity at t=0, the resonant mode should decay exponentially into two ports,

$$\frac{d|a|^2}{dt} = -\left(\frac{2}{\tau}\right)|a|^2 = -(|S_{1-}|^2 + |S_{1-}|^2) = -|a|^2(|d_1|^2 + |d_2|^2) \quad (2.20)$$

which indicates,

$$|d_1|^2 + |d_2|^2 = 2/\tau \quad (2.21)$$

By exploiting time-symmetry, device symmetry and lossless medium assumption, d_1= d_1=d and also κ_1=κ_2=κ and also d=κ can be satisfied if the reference planes are symmetrically placed on each side. Then, the direct transport matrix can be written as:

$$C = e^{\phi} \begin{pmatrix} r & jt \\ jt & r \end{pmatrix} \quad (2.22)$$

where r, t and ϕ are real valued constants associated with reflection, transmission and phase accumulation and also r^2+t^2=1. The values for d_1 and d_2 can be defined as stated in [66],

$$d_1 = d_2 = je^{\frac{j\phi}{2}}\sqrt{r+jt}\sqrt{\frac{1}{\tau}} \tag{2.23}$$

Then, the scattering matrix *S* given in Equation 2.18, can be defined as,

$$S = e^{j\phi}\left\{\begin{pmatrix} r & t \\ t & r \end{pmatrix} - \frac{1/\tau}{j(\omega-\omega_0)+1/\tau}(r+jt)\begin{pmatrix} 1 & 1 \\ 1 & 1 \end{pmatrix}\right\} \tag{2.24}$$

By utilizing the previous equations the final equation for transmission coefficient *T* is found as Equation 2.25.

$$T = \frac{t^2(\omega-\omega_0)^2 + r^2\left(\frac{1}{\tau}\right)^2 + 2rt(\omega-\omega_0)(1/\tau)}{(\omega-\omega_0)^2 + (1/\tau)^2} \tag{2.25}$$

Using Equation 2.25, the transmission power spectra for the generic devices can be extracted that are shown in Figure 2.10:

(b) The device is a side coupled resonator to a PhC waveguide. The scattering matrix *C* for this device without the resonator should be only transmissive so that $C=\begin{pmatrix} 0 & 1 \\ 1 & 0 \end{pmatrix}$ which is possible only when r=0, t=1 and ϕ=-π/2. Then the transmission becomes

$$T = \frac{(\omega-\omega_0)^2}{(\omega-\omega_0)^2 + (1/\tau)^2} \tag{2.25}$$

The plot of this equation is given in Figure 2.10(d).

(c) The device is similarly a side coupled resonator, with an extra rod that is positioned in the middle of the waveguide. This rod creates a Fano interference configuration, such that the different frequencies of light experience different phase accumulations. In this case, both *r* and *t* are somewhere between 0 and 1 depending on the device. For the plot in Figure 2.10(e) they are both selected at 0.5. The middle rod creates a sharp asymmetric resonance where a dip is followed by a sharp peak in a very small frequency range which is called a Fano-resonance [67]. This device

scheme is important since the device that is being utilized in this thesis is heavily inspired by this configuration. The sharp resonance is suitable for sensing applications since it enhances the sensitivity, it is also a promising resonance type for optical switches and all kinds of PhC devices with a resonator [4], [66], [67].

CHAPTER 3

HIGHLY SENSITIVE AND TUNABLE FANO-LIKE ROD-TYPE SILICON PHOTONIC CRYSTAL REFRACTIVE SENSOR

In this chapter, the design procedure of a two-dimensional rod-type silicon PhC cavity is analyzed. The main approach and motivation for this work are presented and the figures of merit are discussed in detail.

3.1 Two-Dimensional PhC Cavity

As it was discussed in the previous chapter, two-dimensional PhCs are created via the periodical arrangement of alternating dielectric materials. These structures can exhibit a band gap where the light is not allowed to propagate in the structure. A cavity can be created by introducing a perturbation, such as a defect or misplacing one of the unit cells. The cavities support a frequency range inside the band gap, thus if somehow, any light that is spatially confined in the cavity, can't propagate to the surrounding structure, and gets trapped inside the cavity. This paves the way of creating sensors since the light is spatially localized and the transmission spectrum becomes highly dependent on the conditions of that resonance frequency. When the device structure is altered by the analyte, the resonance frequency will also be altered, which will result in a sensor in the right configuration and optimization. Here, the design is implemented by using a rod-type PhC configuration using Silicon as the material of choice (n_{Si}=3.48). An example device configuration and its transmission spectrum are given in Figure 3.1(a) and Figure 3.1(b). The 2D PhC structure is constructed via the periodic arrangement of silicon pillars with a square lattice configuration on top of the 2 μm buried Silicon Oxide layer. To eliminate the reduced transmissivity created by the finite length of the rods, the structure is sandwiched between 2 PEC layers to ensure out-of-plane light confinement and to

introduce continuous translational symmetry in that direction to make the effective rod heights infinite [4]. The design parameters were determined by performing multiple photonic band gap simulations with the MPB package. Also, TM polarization is selected to maximize the band gap for rod-type PhC. One row of the rods, except the single one in the middle, is etched to make a line defect PhC waveguide that pulls the modes below the first band to the higher frequencies into the band gap to obtain transmissivity [4]. Then, a point defect cavity is created by etching one of the rods, and that becomes side-coupled to the PhC waveguide, which resides in three rows away from the defect. The lattice period (a) is set to 578 nm, rod radius (r) is set to $0.2a$, and the height of the rods is the same as the lattice period which, will also ensure that flexible tuning without the risk of pull-in phenomenon [68]. Since infinitely long rods are not feasible, to create a similar effect, the rods are sandwiched between two Perfect Electric Conductor (PEC) plates, this is also not feasible for fabrication, so PEC plates are replaced with thin gold layers which will be analyzed later in this chapter. The lattice formation is square lattice so the lattice constant is the same for both x and y directions.

The structure in Figure 3.1(a) possesses a band gap as shown in Figure 2.7(b), for TM polarized light. Removing one rod as a cavity creates an allowed state in the band gap, and light couples to the cavity from the waveguide. Then, it is both spatially and temporally confined in the cavity, and radiates through the evanescent fields. As it is clearly seen in Figure 3.1(b), the transmission decays by one order of magnitude at the resonance frequency, indicating that the light is trapped inside the cavity.

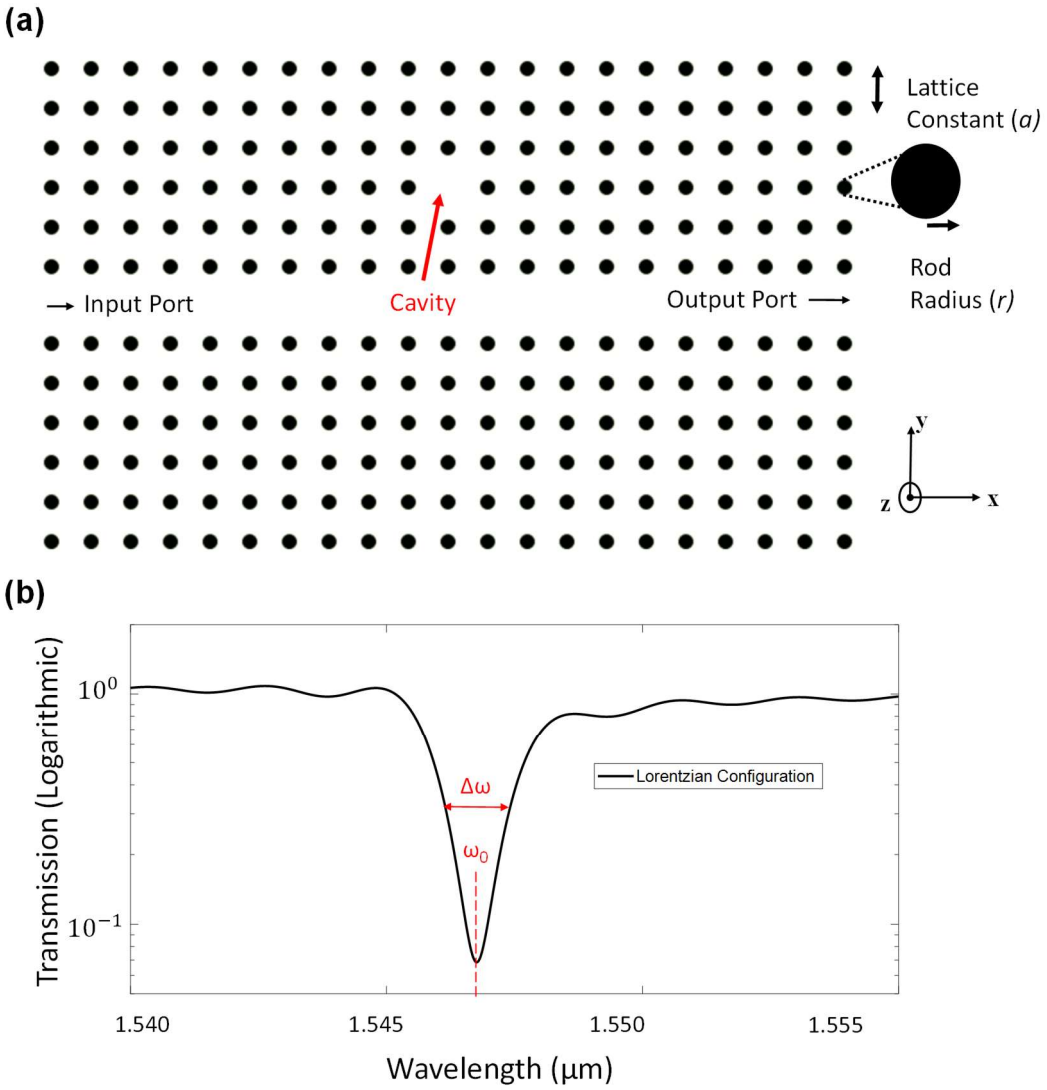

Figure 3.1. **(a)** Schematic of the simulated two-dimensional rod-type PhC. **(b)** The transmission spectrum of the device is shown in **(a)**.

The aim of a refractive index sensor is to maximize the interactions between the field and the analyte to increase sensitivity. Conventional PhC sensors achieve this with the help of the evanescent fields near the silicon. Although it is a very solid and simple solution, it is not as effective as other methods, since the majority of the power is contained within the slab and only a small portion of this power is propagating through to the evanescent fields. To maximize the light matter interaction, studies were directed towards different approaches such as creating a small slot to strongly

localize the light in this area. It significantly boosts the light matter interaction and yields remarkable results [61], [62], [69]. This structures rely on the Maxwell's Equations that the discontinuity of the normal $\boldsymbol{D}$ is equal to the surface charge density. If there are no charges on the boundary, then $\boldsymbol{D}$ must be continuous as in Equation 3.1.

$$\begin{gathered} \boldsymbol{D}_1 - \boldsymbol{D}_2 = \rho_s \\ \boldsymbol{D}_1 - \boldsymbol{D}_2 = 0 \\ \boldsymbol{D}_1 = \boldsymbol{D}_2 \\ \epsilon_1 \boldsymbol{E}_1 = \epsilon_2 \boldsymbol{E}_2 \\ \boldsymbol{E}_1 = \frac{\epsilon_2 \boldsymbol{E}_2}{\epsilon_1} \end{gathered} \tag{3.1}$$

So, the $\boldsymbol{E}$ field can be boosted by the amount of the dielectric constant difference between the material (ϵ_2) and the background (ϵ_1). If the material is selected as silicon and the background is air, the enhancement is around 12 which indicates a very strong localization. However, the slotted structures require a slot with a width of a few tens of nm, an air-bridge structure that requires that the device is suspended in the air, also very high aspect ratios around 80 (length/width). Such an example structure is provided in Figure 2.6(a). The fabrication of such devices is indeed a challenging task. For this case, we have proposed the rod type silicon PhC as a refractive index sensor for the first time. The structure is based on the silicon rods that are sandwiched between perfect electrical conductor (PEC) layers. PEC layers are reflective and it forces the wave vector for the orthogonal direction to become zero. This makes the effective rod heights as infinity and the structure behaves like a two-dimensional PhC as in Figure 3.1(a). For the fabrication, the PEC layers will be replaced by gold layers, which is inspired by Ref. [70]. For this kind of structure, the field is strongly confined in the air so the light-matter interaction is maximized and an ultra-high sensitivity can be achieved.

3.2 Performance Metrics

There are several performance metrics that are commonly used to characterize optical refractive index sensors and PhC cavities. In this part, Q-factor, sensitivity and the mode-volume will be analyzed.

3.2.1 Q-Factor

Q-factor is one of the most commonly used metrics throughout all engineering areas. For resonators and PhC cavities, the Q-factor is a metric for the loss of the resonance. It is a dimensionless quantity that quantifies the center frequency per loss rate [4]. Q-factor determines the sharpness of the resonance peak and dips on the wavelength spectrum. A larger Q-factor means a sharper resonance characteristic. For a refractive index sensor, a high Q-factor is desired since it will increase the minimum detection limit as the Q-factor increases. For a Lorentzian resonance, the mathematical expression can be given as in Equation 3.2.

$$Q = \frac{\lambda_0}{\Delta\lambda_{FWHM}} \tag{3.2}$$

where λ_0 is the resonance wavelength and $\Delta\lambda_{FWHM}$ is the full width at half maximum (FWHM) wavelength.

3.2.2 Sensitivity (*S*)

One of the crucial features of refractive index based bio-sensors is sensitivity, which is the amount of shift in the resonance wavelength per refractive index change represented in Equation 3.3.

$$S = \frac{\Delta\lambda}{\Delta n} \tag{3.3}$$

This parameter is also desired to be maximized since a very small amount of change in the background refractive index means a large shift in the resonance wavelength,

if *S* is large. If the Q-factor is also large, a small shift of the resonance wavelength can mean a significant change in the output power, thus making a higher sensitivity resolution.

3.2.3 Mode Volume (V_m)

Mode volume represents the spatial confinement of the energy inside a cavity region. A smaller mode volume means that the energy is confined in a spatially small region inside the cavity, which can result in an increased light-matter interaction, thus increasing the sensitivity for the resonance. Dense fields can be easily disturbed by small perturbations or molecules, enabling the detection of even single particles [69]. The mode volume calculation can be done using Equation 3.4.

$$V_m = \frac{\int \epsilon |\boldsymbol{E}(\boldsymbol{r})|^2 dV}{\max(\epsilon |\boldsymbol{E}(\boldsymbol{r})|^2)} \tag{3.4}$$

3.3 Design of the Device and Numerical Analyses

As it is stated in the previous chapter, the design of the PhC waveguide is achieved by a linear defect, and the resonance cavity is achieved by a point defect. With the help of band diagrams, the supported modes can be deterministically found and the design procedure should start with finding the supported modes and frequencies for the device structure and adjusted them to the desired wavelength which is 1550 nm for this work. To maximize the light-matter interaction, the propagating mode is confined in the low index material (which is air), on the contrary to the conventional devices which confine the light in the high index material, which is mostly Silicon.

3.3.1 FDTD and Band Gap Analyses

The band diagram of a two dimensional PhC structure with silicon rods is given in Figure 2.7(b), the TM polarized input is selected since it possesses a relatively large

band gap, which is something required for this type of application for both high Q-factor and transmission depth for the resonance cavity. The effect of the line defect (PhC waveguide) can be simulated by MPB by creating a super lattice 7x1 still using the same periodicity for the defects. The radius of the rods is chosen as 0.2*a*, where *a* is the lattice constant. The supported modes for guiding are shown with orange line in the band diagram that is given in Figure 3.2. The light gray regions indicate the band gap and the blue regions are the allowed extended modes inside the PhC. The group velocity for the allowed modes can be found by taking the derivative of the angular frequency with respect to the angular wavenumber, which corresponds to the slope of the orange line in Figure 3.2. It is an important parameter to reduce the losses and increase the Q-factor in the next step, which is creating the cavity.

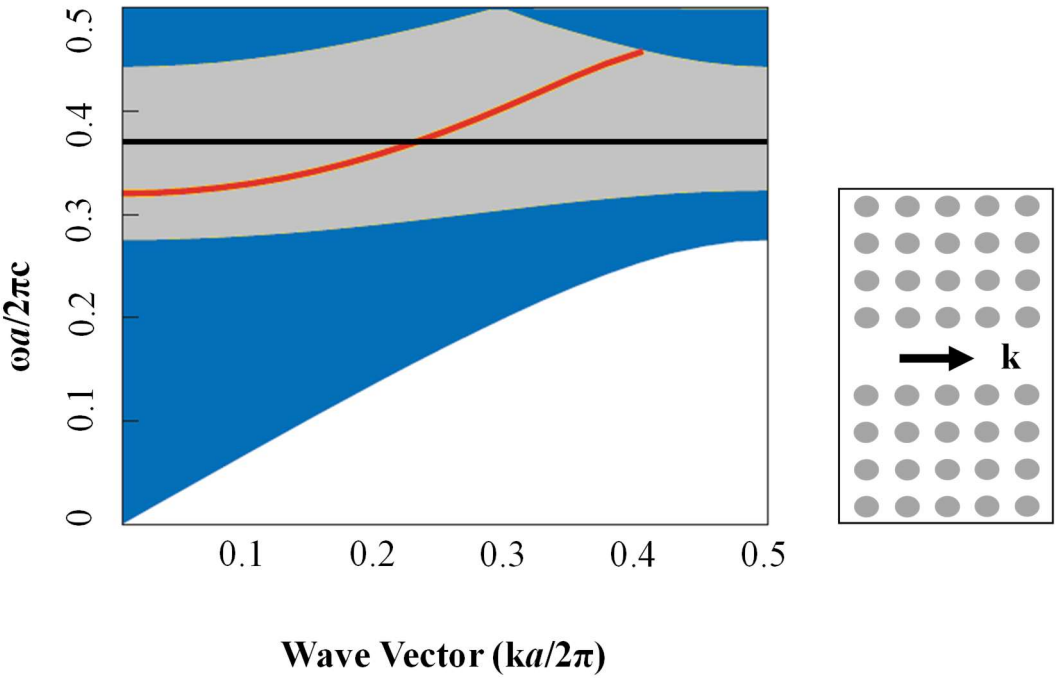

Figure 3.2 The projected band diagram of the PhC with square lattice of rods. Orange line indicates the allowed modes introduced to the band gap by the linear defect, and the black line indicates the allowed frequency of the resonance cavity.

To find the effect of the line defect, another super lattice is created but this time, it has a size of 7x7 with the defect in the middle. As shown in Figure 3.2, the black line represents the effect of the point defect which is the cavity. The intersection point of

the orange line and the black line shows the exact wavelength of the resonance for the cavity which is selected as 1550 nm when the lattice period is selected as 571 nm, also the Q-factor and the transmission of the cavity is directly correlated with the slope of the orange line at the intersection point.

The mode profile and the transmission spectrum for this device are already shown in Figure 3.1. This design has a Lorentzian resonance which is one of the most common resonance characteristics. However, for this work, it is not the ideal type of resonance since sensitivity and Q-factor is some of the most important parameters for a bio-sensor. Instead, the structure is modified and a Fano-like resonance characteristic is achieved. Fano-like resonances are sharp and asymmetric resonances usually have a lower transmission level than Lorentzian types but they make that up by providing a much higher Q-factor. The modified structure is presented in Figure 3.3. As it can be seen from Figure 3.3**(b)** the transmission characteristics is changed from Lorentzian resonance to Fano-like resonance. The two designs appear nearly identical with the exception of the rod that is stationed in the middle of the waveguide at the same x-axis location with the point defect. This changes some important things in the transmission spectrum. Firstly, the rod that is placed acts like a partially transparent mirror, and reflects some of the incoming waves back to the input port. This causes a decrease in the total amount of energy that is reaching the output port, thus decreasing the maximum amount of transmission by around 2.5 dB. However, it has significant benefits to the design. Firstly, it creates the sharp and asymmetric Fano-like resonance characteristics, which is inherently sharper than the Lorentzian resonance, which means it has a higher Q-factor. The importance of the Q-factor is stated in Chapter 3.2.1. Basically, it makes the sensor more sensitive to the external effects and even with a slight shift on the background refractive index, the transmission level can be switched from the maximum state to the minimum state(or close to a minimum depending on the shift). Another thing that happens is that the transmission depth is greatly increased. The difference between the transmission depth of the Lorentzian-like cavity and the Fano-like cavity is nearly 30 dB.

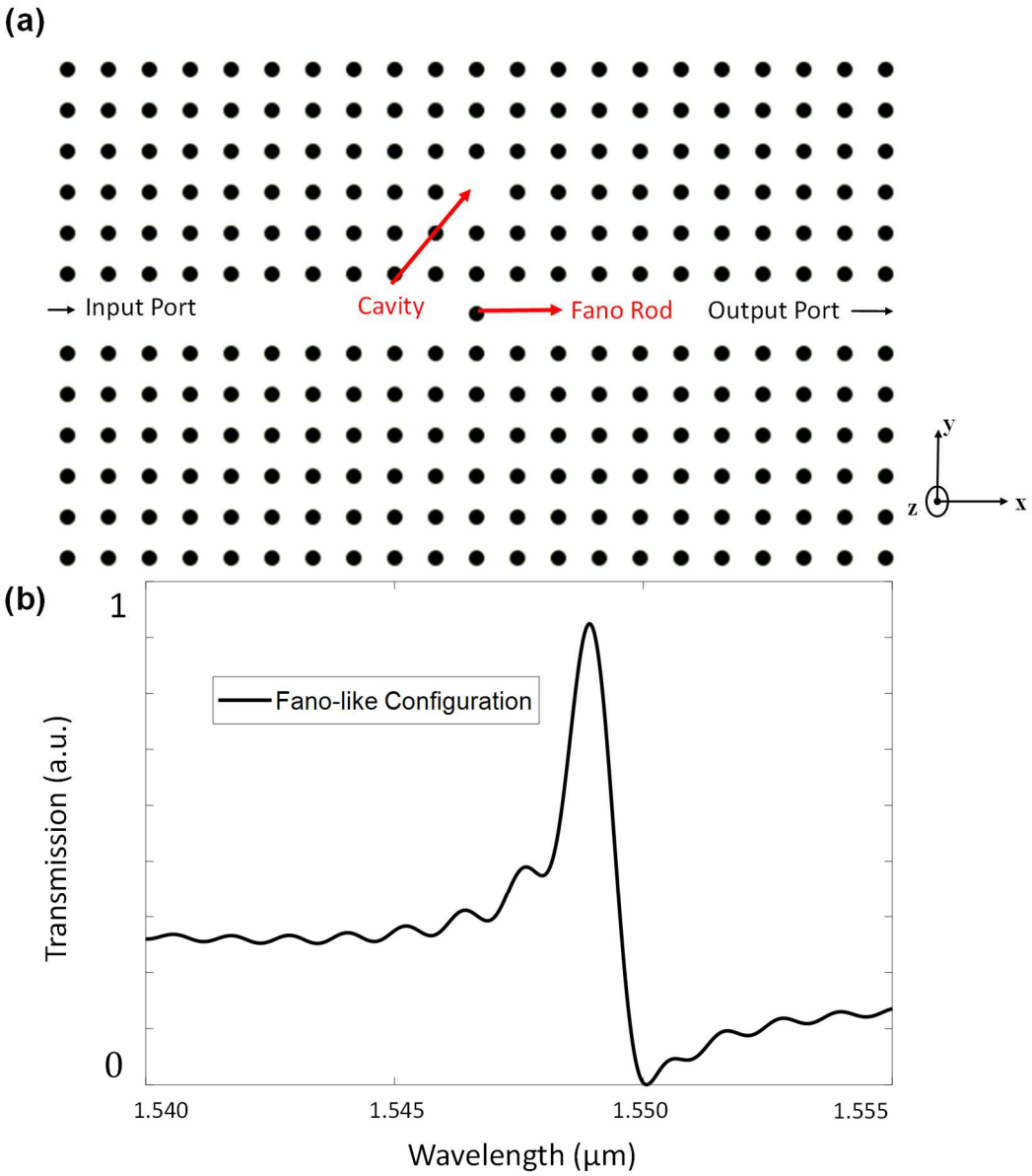

Figure 3.3 **(a)** Schematic of the simulated two-dimensional rod-type PhC after the insertion of the Fano rod. **(b)** The transmission spectrum of the device that is shown in **(a)**.

The main structure of the device is chosen as given in Figure 3.3**(a)**. However, each performance metric should be optimized accordingly for this device. So a numerical comparison between the Lorentzian resonance type structure and Fano-like resonance type structure is necessary.

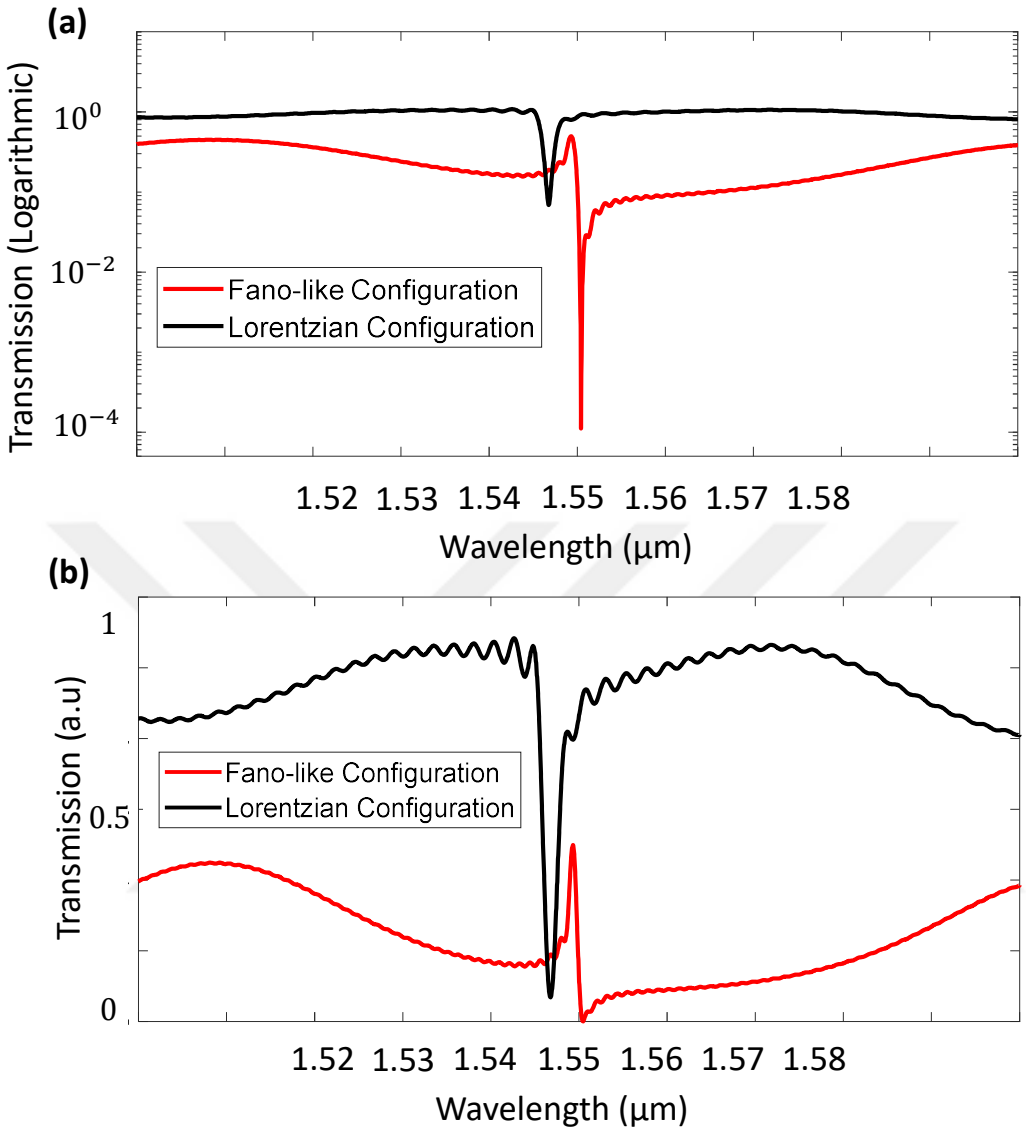

Figure 3.4 The transmission spectrums of Lorentzian Configuration and Fano-like configuration. **(a)** Logarithmic scale. **(b)** Linear scale.

A comparison of both device configurations is shown in Figure 3.4. As it is explained before, the Fano-like configuration has a smaller peak transmission level, but it compensates this from the higher Q-factor and extended transmission depth. This might not be obvious if the graphs were analyzed in the linear scale. However, most of the analyses in integrated photonics and are conducted using logarithmic scale and the difference is obvious in Figure 3.4**(a)**. The Fano-like resonance offers sharp asymmetric resonance characteristics that are suitable for a sensing device as stated

before. The presence of the rod in the middle of the PhC waveguide changes the transmission characteristics to a Fano-like one from a conventional Lorentzian one. This conversion improves the extrinsic Q-factor of the cavity to 2231 from 1346 and the transmission depth to 43 dB from 11 dB. However, this improvement comes at the cost of a 3 dB reduction from the peak transmission, as shown in Table 3.1. Fano resonance in general can be observed when the direct coupling is not perfect (partially reflective rod in the middle of the cavity creates this), one obtains an asymmetric spectrum of a sharp peak followed by a sharp dip as previously shown. The sensing is improved in this situation because of the nature of the sharp peak followed by the sharp dip. Fundamentally, the sensitivity value of the device is not affected that much. However, the resolution of the minimum amount of refractive index change is improved. It is easier to reach the dip from the peak or vice versa compared to the same device with Lorentzian resonance characteristics.

Table 3.1 Comparison of Lorentzian and Fano-Like resonance type devices

Resonance Type	***Q-Factor***	***Transmission Depth***	***Relative Insertion Loss***
Lorentzian	1346	10.3 dB	0 dB
Fano-Like	2231	41.2 dB	3 dB

After setting the design parameters and optimizing them, one of the most important performance metrics, the sensitivity of the device needs to be investigated.

Every material interacts with the light differently based on their permittivity. This interaction is based on complex refractive index, which can be seen as an analogue of impedance in electronics.

$$\epsilon = (n + i\kappa)^2 \tag{3.5}$$

In Equation 3.5, the complex permittivity (ϵ) is written in the complex form. n is the refractive index and κ is the extinction coefficient [54]. For electromagnetic waves

with 1550 nm wavelength, the atmosphere is nearly lossless and the refractive index is very close to 1. The sensing is achieved when the resonance frequency of the cavity is shifted. Initially, the background refractive index is constant and the device is designed according to it. When the analyte (gas in this analysis) is introduced, the refractive index of the background increases. This increase changes the resonance frequency based on the sensitivity value of the device. If the shift is large enough, a detector from the output signal can shift since the light intensity at the output shifts from peak-to-dip or vice versa.

To begin the analysis, a suitable simulation environment is modeled for gas detection. The structure is analyzed with the 3D FDTD method using MEEP package [59].

The ambient pressure is initially selected as standard atmospheric pressure, and the temperature is set to the room temperature 300 K. The background material is selected as air, then, simulations were performed for several different background gases like Acetylene, Chlorine, and SF6 that can be seen in Figure 3.5**(a).** The change of the refractive index shifts for each material is based on some of the previously published experimental results [71], [72]. After the FDTD simulations, it is observed that a background refractive index shift of 10-4 RIU corresponds to a 103.9 pm shift in the resonance wavelength. So the sensitivity of this device can be calculated from Equation 3.3 is 1039 nm/RIU. Since only a few data points from three samples is not enough to get a solid assumption, more hypothetical data points are added to extend the simulation range and to increase the resolution and the shift in the resonance wavelength with respect to the background refractive index shift is shown in Figure 3.5**(b)**. Thanks to the sharp asymmetric Fano-like resonance and relatively high Q-factor, the minimum detectable refractive index shift is found to be 2.76x10-4 RIU which is sufficient for detecting many different gasses [71]. The sensitivity resolution benefits from the asymmetry of the Fano resonance since we operate in the region where a sharp peak is followed by a sharp dip. This enables that even a relatively small amount of shift leads to a detectable change in the transmission compared to the same device with the Lorentzian resonance characteristics.

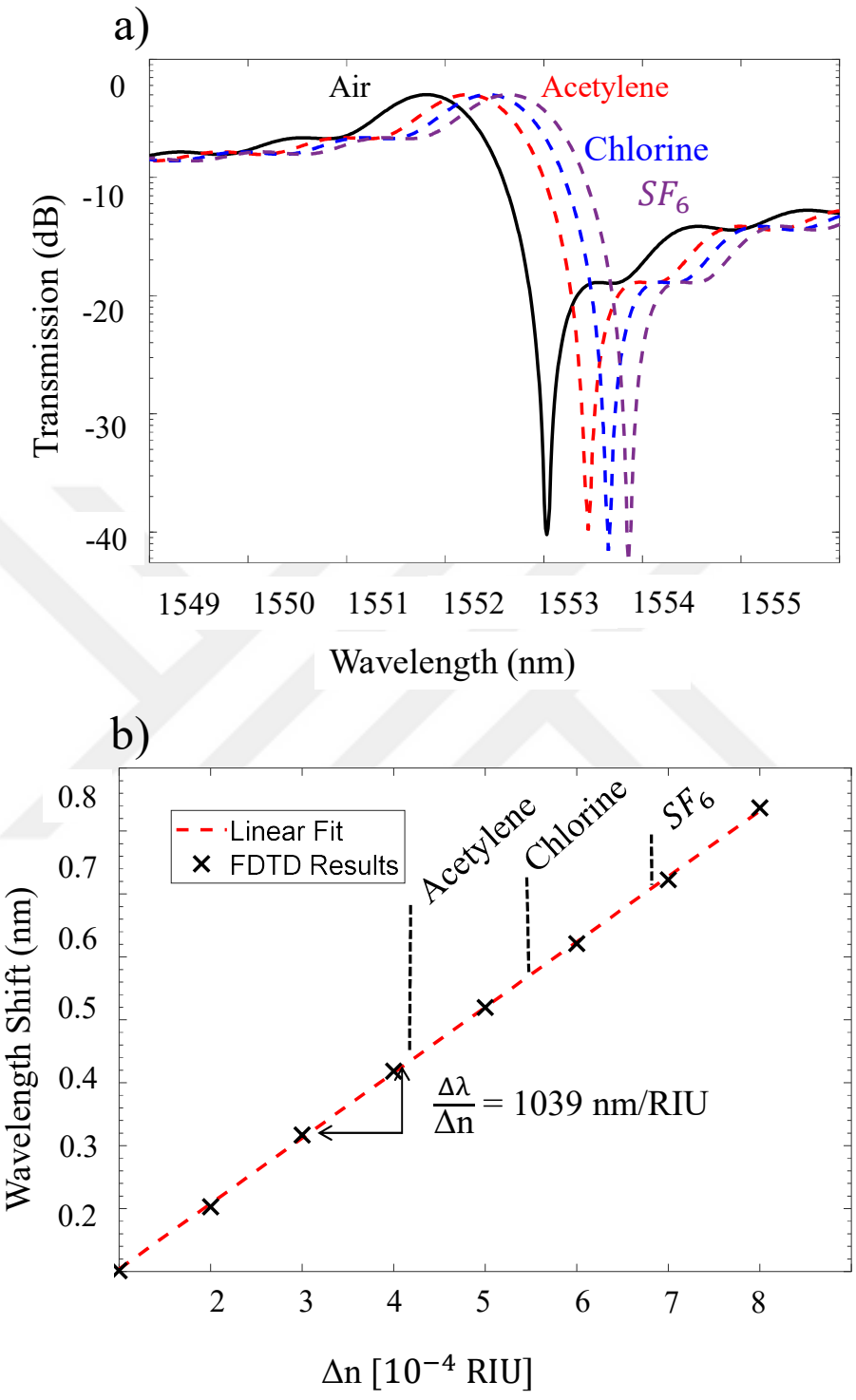

Figure 3.5 **(a)** Transmission spectrum when different gases are introduced in the simulation environment, from left to right: Air, Acetylene Chlorine and SF_6. **(b)** Plot of wavelength shift per change in the background refractive index. The sensitivity value is found as 1039 nm/RIU.

Another performance parameter for optical biosensors is the response factor (R), which is the ratio of normalized wavelength and refractive index given in Equation 3.6. [71].

$$R\frac{\Delta n}{n} = \frac{\Delta \lambda}{\lambda} \tag{3.6}$$

Response factor is one of the figure of merits that is being used for optical biosensors. The response factor is calculated as 0.66, which is among the highest recorded values in the literature.

When the background index changes, the index contrast between Silicon rods and the background also changes and this has some effects on transmission and Q-factor. However, since for gas detection, Q-factor variation with respect to the background refractive index shift is negligible even on the order of 10-2 RIU shifts, so it can be stated that the Q-factor is independent of the background refractive index in the desired operation range as is it shown in Figure 3.6.

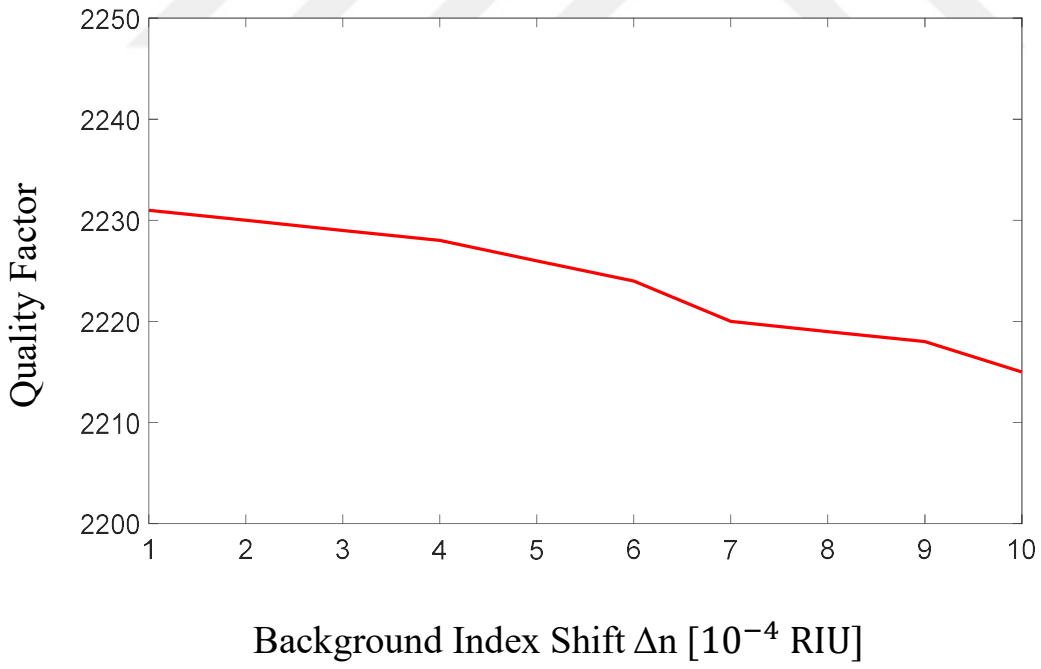

Figure 3.6 Variation of Q-factor with respect to background index shift

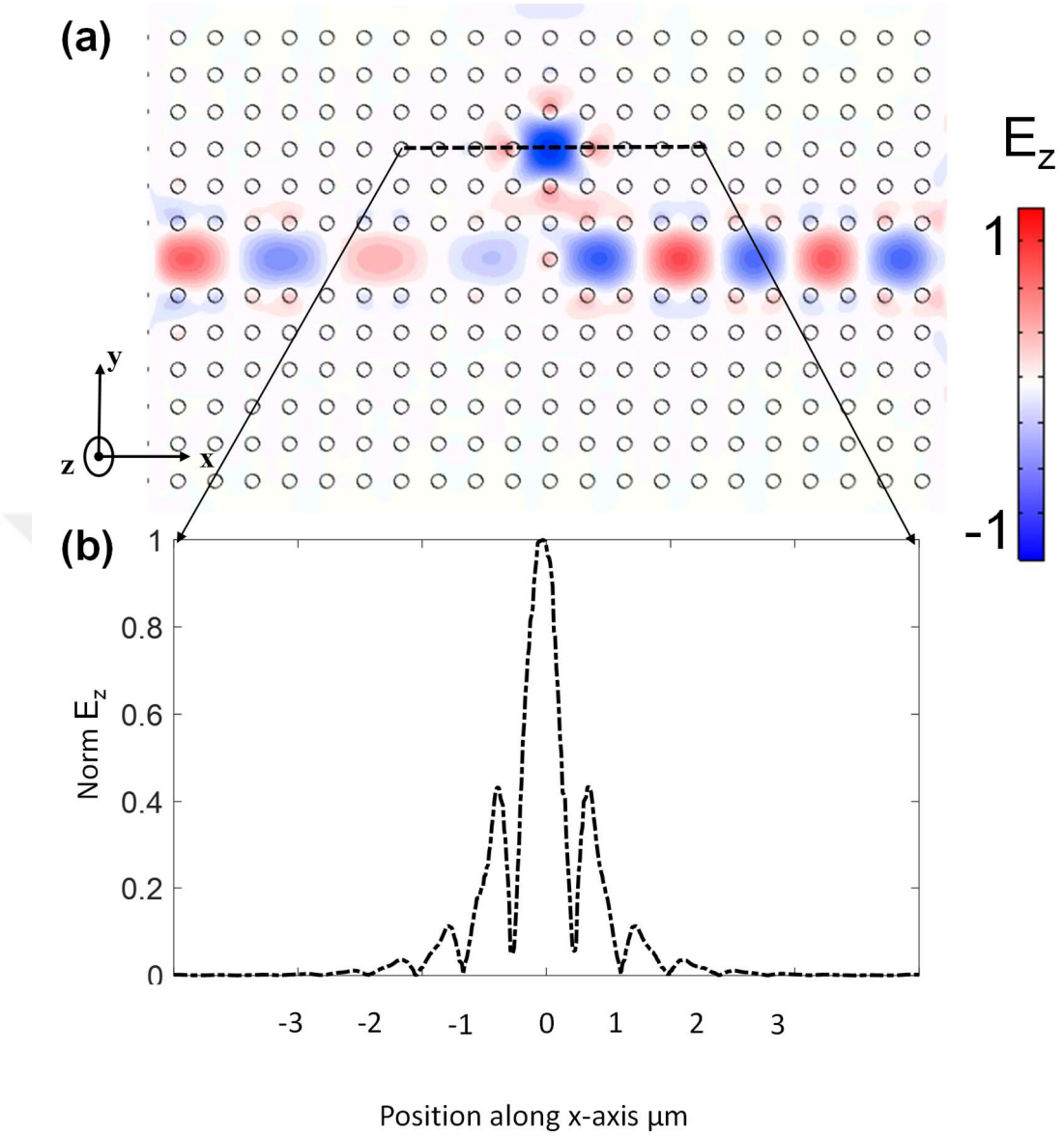

Figure 3.7 FDTD analysis of the structure **(a)** Ez mode profile of the fundamental resonance of the cavity. **(b)** Normalized Electric Field (Ez) Slice of the cavity area.

The mode profile of the fundamental resonance for TM-like excitation is given in Figure 3.7**(a)**. The electric field couples to the cavity and traps inside it, at the same time other frequency components continue to travel inside the cavity. If excited for a single wavelength source, like a laser, with a carefully selected wavelength, majority of the light can be trapped inside the cavity or it can directly couple to the output. To extract the numeric E-field data, a line slice is taken through the cavity in

the direction of propagation and it is shown in Figure 3.7**(b)**. The data from Figure 3.7**(b)** is taken from FEM analysis so it is seen that both methods are consistent with each other. As it is seen from Figure 3.7**(a),** the electric field is spatially confined inside the cavity region. However, mode volume is relatively large since the field is not confined in a spatially small region. Using Equation 3.4, the mode volume for this device configuration is calculated as 1.33 $(\lambda/n)^3$. Although this value is relatively small, subwavelength confinement is not achieved. In the next part of this chapter, a new method for both shrinking the mode volume and an external and electrical method for tuning the resonance wavelength will be presented.

Another important parameter that can be used for a figure of merit (FOM) for comparing different types of devices is the sensitivity over full width at half maximum (S/FWHM). The proposed device has a FOM of 748 with the PEC plates.

The most important performance metrics for the device with PEC plates and without the insertion of air-gap are presented in Table 3.2. These values will be modified after the insertion of the air-gap for tuning, and also loss will be increased when PEC plates will be replaced with gold plates. Their analysis will be conducted in the next part.

Table 3.2 Performance Metrics of the device with PEC plates (without gap insertion)

Performance Metric	**Value**
Q-factor	2231
Sensitivity	1039 nm/RIU
Mode Volume	1.33 (λ/n)3
Response Factor	0.66
S/FWHM	748

3.3.2 Insertion of Air-Gap and FEM Analyses

FEM analysis is done via COMSOL Simulation Environment. Further investigations had to be made with COMSOL since MEEP can't efficiently simulate plasmonic effects that will be introduced by gold layer (which is the replacement of PEC layers) and also correctly simulating the smaller feature sizes requires a high resolution which multiplies the required computation power eight times since it will be a 3-D simulation. Meshing is automatically controlled by COMSOL. The sharper and smaller features that require finer mesh size are automatically calculated and continuous and larger areas that would make an accurate solution with coarser mesh sizes are calculated to be larger. An example representation of a similar structure is given in Figure 3.8. It is seen that the mesh sizes are smaller when feature sizes become smaller and require smaller mesh sizes and similarly, mesh sizes are larger when the structure has homogenous and bulkier parts.

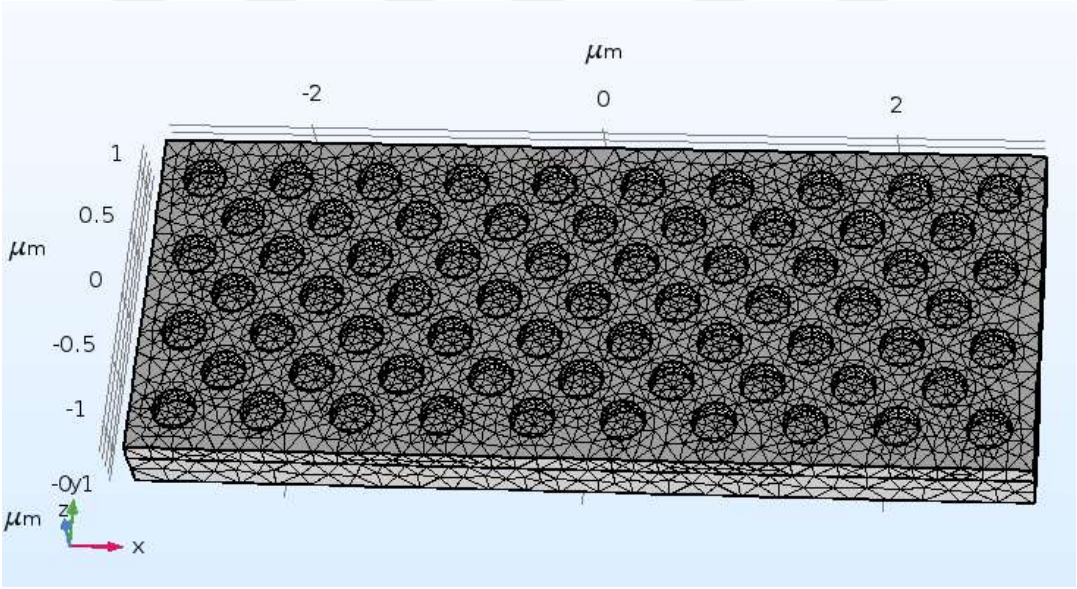

Figure 3.8 Mesh structure of a 2D PhC via COMSOL

To tune the resonance frequency of the cavity, an air gap is introduced to the cavity and it is mechanically perturbed via electrostatic actuation between two parallel plates, a well-known phenomenon for MEMS applications. Air gap insertion also decreases the effective permittivity of the resonant modes. So the modes undergo an upper shift on the frequency. The CAD drawing of the resultant structure after air gap insertion is given in Figure 3.9. In Figure 3.9**(a)** an isometric view of the structure and its dimensions and used materials are provided. Dark grey areas represent Silicon, light grey areas represent SiO_2, and the yellow areas represent PEC layers. PEC layers will be replaced with gold so they have a golden like color in the illustration. As it is seen from Figure 3.9**(a)** the device is relatively small for a biosensor and only span on an area of 5.52μm x 10.64μm. In Figure 3.9**(b)** the cross sectional view of the structure is given, as can be seen from the figure, the air gap is inserted on top of the Silicon rods. There are two conductive layers and they make a parallel-plate capacitor since they have a dielectric region between them. If an electrical voltage is applied between the top and bottom plates, they exert a force, since the bottom plate is stationary, and the top plate is designed like a membrane structure it can move and the direction of motion is also given in Figure 3.9**(b)**.

The exact force and voltage needed to move the plate will be calculated later in this part. First, the effect of an air gap on the resonance frequency will be analyzed. The shift in the resonance frequency is predicted by the perturbation theory is given in Equation 3.7 [4].

$$\Delta\omega = -\frac{\omega}{2}\frac{\int d^3\boldsymbol{r}\Delta\epsilon(\boldsymbol{r})|\boldsymbol{E}(\boldsymbol{r})|^2}{\int d^3\boldsymbol{r}\epsilon(\boldsymbol{r})|\boldsymbol{E}(\boldsymbol{r})|^2} \tag{3.7}$$

where, $\epsilon(\mathbf{r})$ and $\boldsymbol{E}(\boldsymbol{r})$ are the vector representations of the permittivity and the electric field and ω is the frequency of the wave. An infinitesimal change in the permittivity vector, which is the gap-size of the air slot region changes the resonance frequency and gives the opportunity to tune the resonance wavelength of the cavity. However, an infinitesimal change in the out-of-plane direction the equation can be written as;

$$\frac{d\omega}{dz} = -\frac{\omega}{2}\frac{\int d^3\boldsymbol{r}\frac{d\epsilon(\boldsymbol{r})}{\boldsymbol{dz}}\,|\boldsymbol{E}(\boldsymbol{r})|^2}{\int d^3\boldsymbol{r}\epsilon(\boldsymbol{r})|\boldsymbol{E}(\boldsymbol{r})|^2} \tag{3.8}$$

Since the gap is very small, the electric field can be assumed constant inside the gap and if all of the electric field is assumed to be confined inside the air gap region, the equation can be simplified as;

$$\Delta\omega \cong -\frac{\omega}{2}\frac{\int dz \int (\epsilon_{air} - \epsilon_{Si})\,|\boldsymbol{E}(\boldsymbol{r})|^2 d^2\boldsymbol{r}}{\int dz \int \epsilon_{Si}\,|\boldsymbol{E}(\boldsymbol{r})|^2\, d^2\boldsymbol{r}}$$

$$\Delta\omega \cong -\frac{\omega}{2}\frac{d_{gap}(\epsilon_{air} - \epsilon_{Si})}{h_{rod}} \tag{3.8}$$

where d_{gap} is the dimension of the gap on the z-direction and h_{rod} represents the rod height.

Initially, it can be assumed that the minimal changes like 5-10 nm differences couldn't have a drastic effect on the resonance wavelength since the distance between two plates is around 780 nm. However, this is incorrect since with the introduction of the air gap, the electric field is strongly confined in this region as illustrated in Figure 3.10. As it can be seen from the figure, when the air gap is inserted, the device acts as a slot structure as discussed in Chapter 2, and to obey Maxwell's Equation boundary conditions, the electric field is strongly confined in the low-index region. The numerical data confirms this as the normalized electric field slice has its peak at the top of the Silicon rods near the point defect as shown in Figure 3.10**(b)**.

The mode volume is recalculated for the device after the insertion of air gap, and it is found as 0.214 $(\lambda/n)^3$ which confirms the sub-wavelength confinement and an improvement by the factor of 6 from the device that doesn't have an air gap.

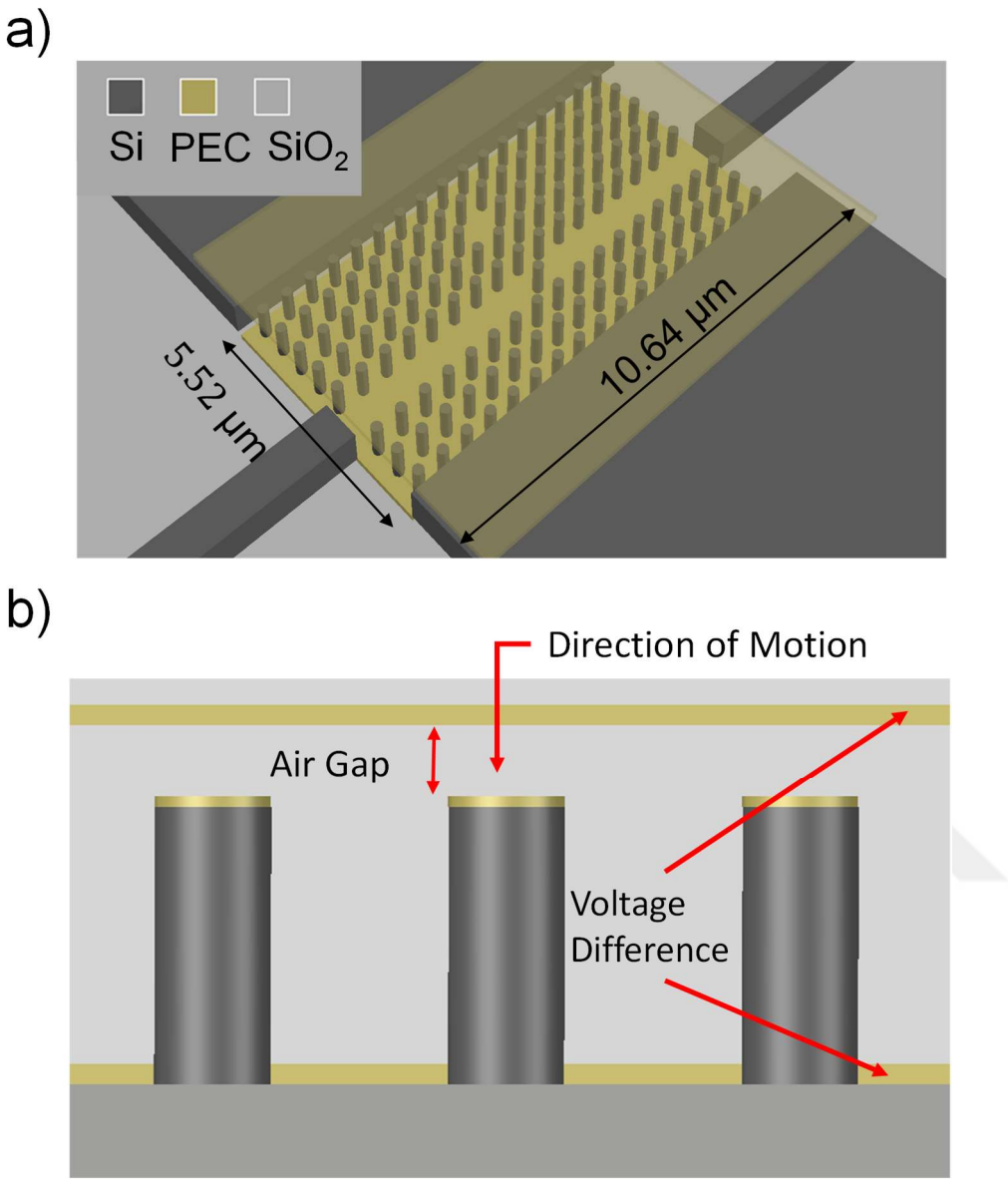

Figure 3.9. 3D CAD drawing of the structure. **(a)** Isometric view **(b)** Cross-sectional view.

The cavity mode profile is not Gaussian after the insertion of the air gap as shown in Figure 3.10**(b)**. Theoretically, it decreases the Q-factor; however, this difference has a very small effect of the device performance since the detection limit doesn't change as it will be shown and the benefits of creating such a highly localized electric field are huge as it is previously stated in this chapter.

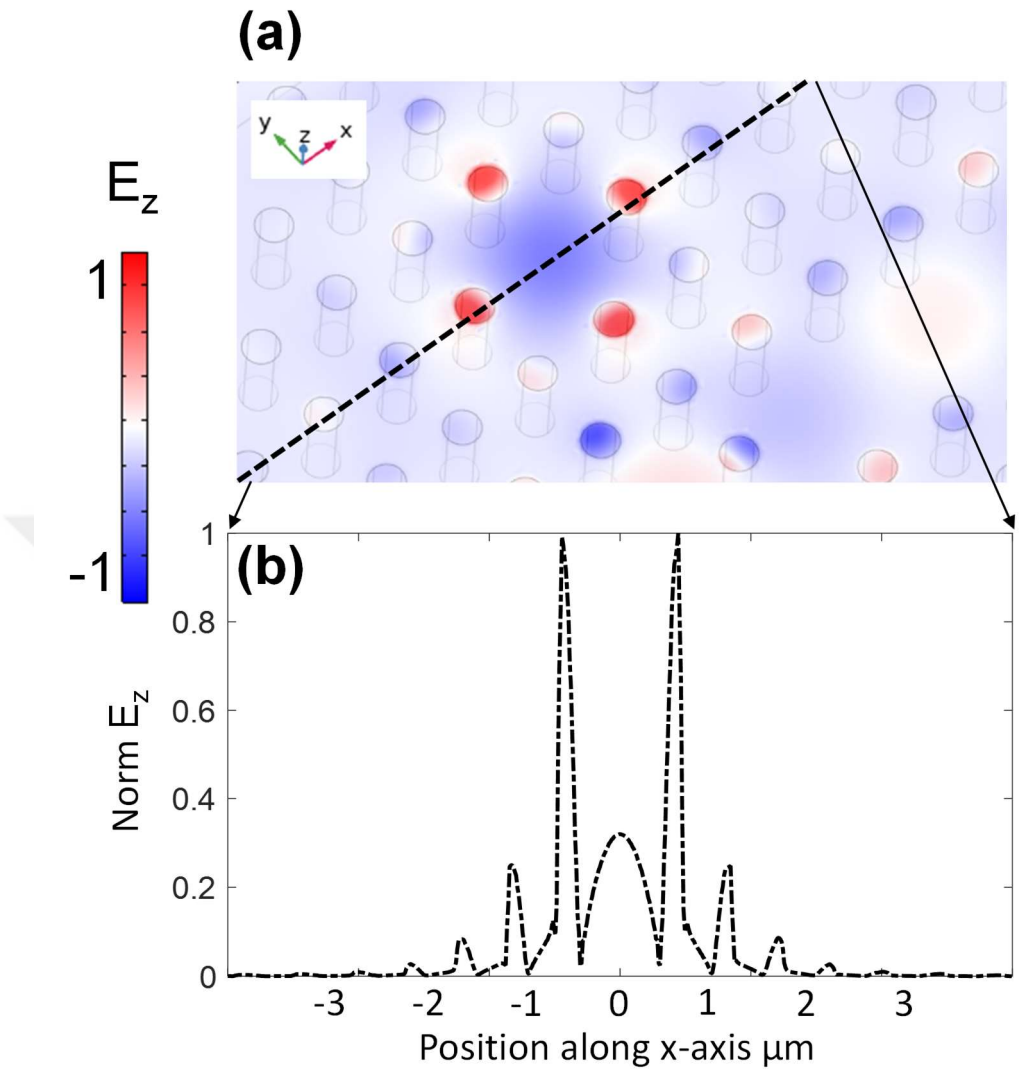

Figure 3.10. **(a)** Cavity Resonance Electric field profile when an air gap of 50 nm is inserted. **(b)** Electric field slice from the center of the cavity along the x-axis.

3.3.3 Replacing PEC Plates with Gold

In the previous parts, the silicon rods are sandwiched between two PEC layers to introduce continuous translational symmetry in the out-of-plane direction to make the PhC behave like a true 2D PhC. PEC layers reflect 100% of the incoming electromagnetic waves regardless of their frequency since they are just models for simulations and have a purely imaginary refractive index. However, in practice, there

is no such material. Since metals are known to be good reflectors, a metal with a high plasma frequency should be selected to maximize the reflection for the desired wavelength of 1550 nm. The complex permittivity of metal can be found from the Drude-Lorentz model given in Equation 3.9 [73].

$$\epsilon(\omega) = \epsilon_\infty - \frac{\omega_D^2}{\omega^2 + i\gamma_D\omega} - \frac{\Delta\epsilon\omega_L^2}{\omega^2 - \omega_L^2 + i\gamma_L\omega} \tag{3.9}$$

where ω_D represent the corresponding metal's plasma frequency, ω_L is the plasma frequency that is associated with the intraband transitions, $\Delta\epsilon$ is the oscillator strength, ϵ_∞ is the relative permittivity for the high-frequency components, and γ is the damping factor for the electrons on the surface of the corresponding metal and it is the same unit as ω.

Fresnel Equations states that the reflection can be 100% if the refractive index of a material is purely imaginary [54]. This is impossible for the real materials since they have both real and imaginary parts, so the aim is to minimize the real part of the refractive index or find a material the real component of the refractive index is much smaller compared to the imaginary part of it, and also a metal that can be used for fabrication for such components. After a literature survey, it is decided that Gold provides those properties better than most metals, and for fabrication, feasibility, and stability, it is chosen as the replacement of PEC layers [70]. However, since the real part of the refractive index of Gold is not zero, there will be losses in the transmission value and Q-factor. To simulate the effects of Gold, especially to observe plasmonic related issues and obtain accurate results, the device is modeled in the COMSOL simulation software. Replacing PEC layers with Gold introduces an insertion loss of 6.7 dB per plate which is a drastic change and it is inherently the case for those types of devices [70]. However, the extinction ratio is still confidently larger than 10 dB which is sufficient for detection. Also, during fabrication processes, the deposited Gold layers will not be perfectly flat, and there can and will be surface roughness. To model those effects in the simulation environment, an intentional surface deformity of periodic 10 nm variations was included in the surfaces of the gold layers. This deformity also decreases the transmission level and the reflection

coefficient. Therefore, Gold adds a new loss component and becomes the dominant loss factor of the device. The new Q-factor with gold plates, whose thickness is 50 nm, is calculated as 487. However, the device can still sense a refractive index shift of 8.45 x10^{-4} RIU due to the ultra-high sensitivity value. The final transmission spectrum after replacing PEC plates with gold layers is given in Figure 3.11.

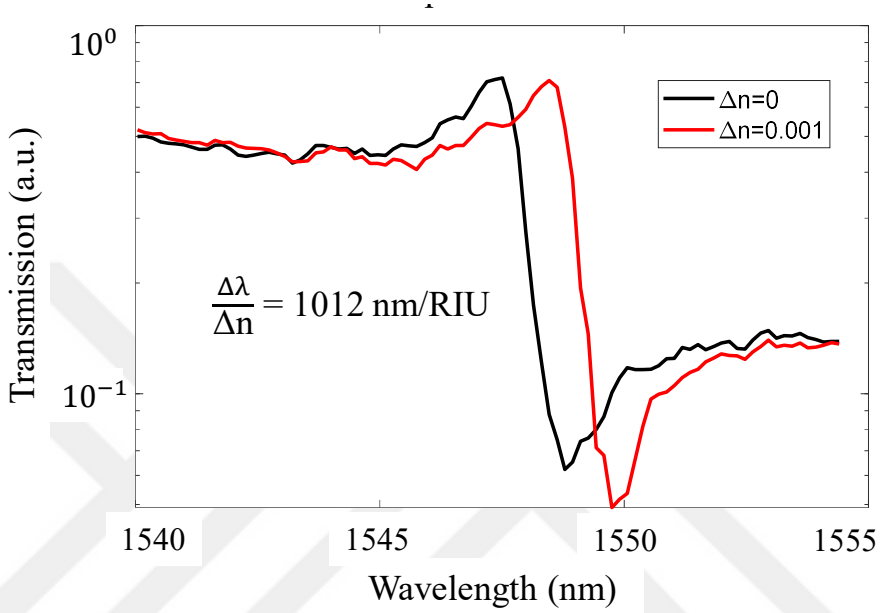

Figure 3.11 Transmission spectrum of the device after replacing PEC plates with Gold plates with varying background indices. Q-factor is calculated as 487. The black line represents the background as air and the red line represent a 0.001 shift in the background refractive index.

Figure 3.11 also shows that a change of 0.001 RIU in the background refractive index corresponds to a change of light intensity from a dip to a peak or vice versa. This confirms that after the replacement of gold, the device is still able to detect the majority of the gases [71].

3.3.4 The Tuning of the Device

The tuning of the resonance characteristic is done by placing the top metal layer 100 nm above the top of the rods during the fabrication process and then pulling it by electrostatic actuation to a few tens of nm by applying a voltage to the top and bottom

metal layers. Analysis of the gap-size and transmission spectrum were performed with COMSOL simulation environment. First, the transmission spectra for different gap sizes and their resonance shifts under the same amount of change with the background refractive index are given in Figure 3.12.

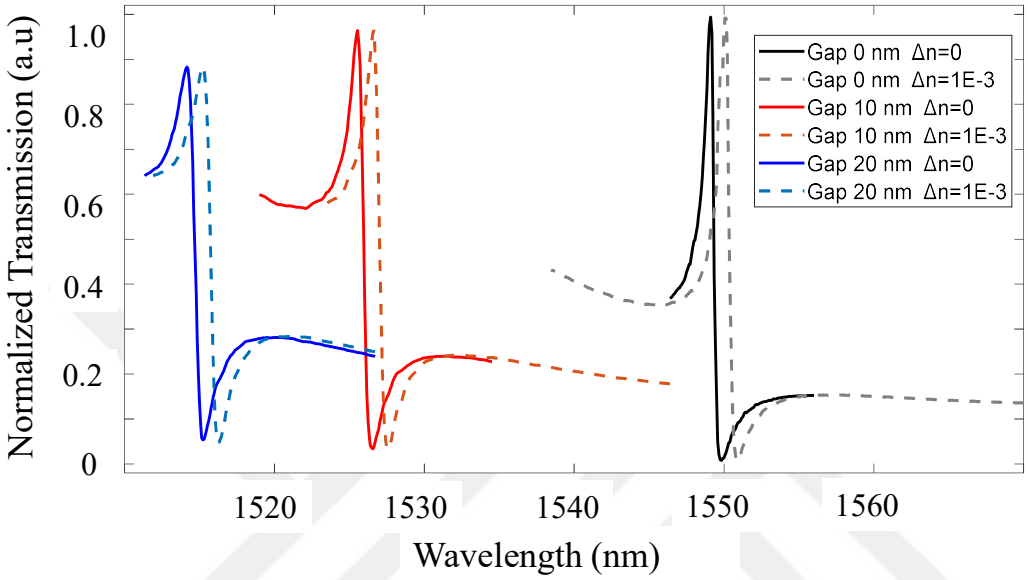

Figure 3.12. The transmission spectra of the device for varying gap sizes and background refractive indices. The simulation environment where the background is air is plotted with solid lines and the dashed lines represent the background index shift of 10^{-3} RIU.

The movable metal plate is placed 100 nm away from on top of the Silicon rods and this distance can further be reduced to a few nanometers depending on the calibration and quality of the experimental system. The top plate is modeled as a metal diaphragm and the bottom plate is assumed to be stationary. In Figure 3.12, it is seen that the dependency of the resonance wavelength to the gap size is huge thanks to the strong localization of the E-field in the air-gap region, which allows the tuning of the resonance frequency of in a flexible and reliable manner. Since the gap acts as a slot structure, the size of the gap has a strong effect on the resonance wavelength; however, it also affects the Q-factor.

Table 3.3 Resonance Wavelength, Q-factor and extinction ratio variations for various gap sizes

Gap Size (nm)	Resonance Wavelength	Q-factor	Extinction Ration
0	1550	2242	28.2 dB
5	1538	2138	22.4 dB
10	1527	2095	21.7 dB
15	1521	2043	17.8 dB
20	1515	2034	16.2 dB
25	1511	2029	14.3 dB
30	1508	2017	13.6 dB
40	1503	2008	11.7 dB
50	1500	1997	10.1 dB

By inspecting Table 3.3, it can be seen that the resonance wavelength changes almost linearly with respect to the gap size after gap size reaches above 10 nm. Also, Q-factor decreases with increasing gap size. Due to this decreased Q-factor and extinction ratio, it is logical that the device should be operated around 1500 nm wavelength, which restricts the maximum gap size to not be larger than 100 nm. Therefore, the tuning range is specified as 50.4 nm or 6.24 THz to preserve the Q-factor around 2050 and transmission depth to be at least 10 dB. However, this value can be increased depending on the quality of the fabrication and tuning configuration. It is clear that as the gap size increases, both transmission depth and Q-factor decrease as expected. An increase in the gap size reduces the effective refractive index of the unit cell of the PhC structure, and this reduced effective refractive index (n_{eff}) induces a blue-shift in the resonance wavelength. Since the background is air, any analyte that is introduced to the environment increase n_{eff} and it creates a red-shift. This allows to create a balanced state, and the tuning can be arranged such that even for very large refractive index variations, the device can still operate at 1550 nm. It is evident that the resonance wavelength shift due to a change in the gap size is much larger than the one induced by the shift of the background

refractive index as shown in Figure 3.12. Since they have opposite effects of each other and the gap size can be precisely controlled, and also the variation range of the refractive index is limited; the balance can be achieved after a calibration process. This property can be utilized for not only the detection of gases but also airborne pathogens and mono-cellular life forms. Single-particle detection with this design is possible only in theory since, in practice, it would be a very complicated procedure to position a particle in the gap region of the cavity. The device can operate in an aqueous environment; however, Q-factor decreases by one order of magnitude due to the reduced permittivity contrast between the silicon rods and the environment. The reason behind this is, by their nature, 2D rod-type PhCs are much more sensitive to the changes in the low-index region, and it enables the high detection limits without depending on a Q-factor on the order of 10^6.

3.3.5 Electrostatic Actuation of the Two Metal Plates

In this part, the voltage required for moving and tuning the distance between a parallel plate capacitor is analyzed. An illustration of the resultant parallel plate capacitance structure is presented in Figure 3.13.

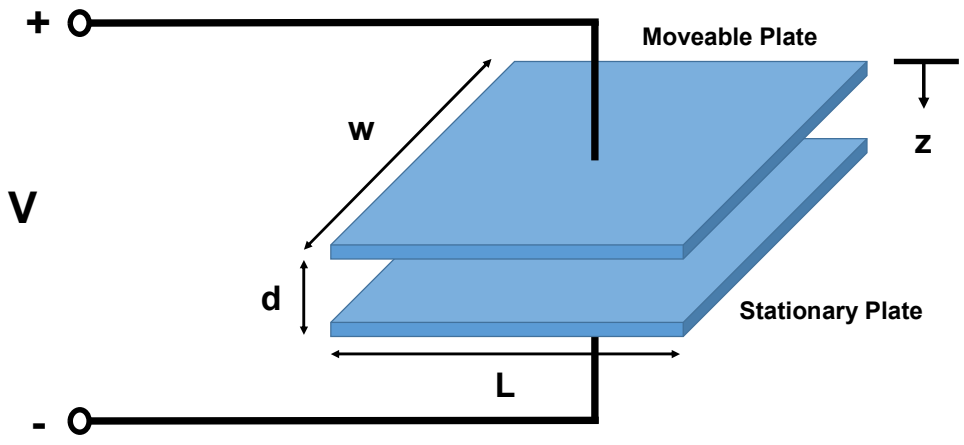

Figure 3.13 Illustration of the device as parallel plate capacitance for resonance tuning.

The capacitance between two plates can be expressed as in Equation 3.7.

$$C = \frac{\epsilon wL}{d} = \frac{\epsilon_0 \epsilon_r A}{d} \tag{3.7}$$

where d is the distance between two plates, A is the overlapping plate area, ϵ_0 is the dielectric constant of air 8.854×10^{-12} F/m, and ϵ_r is the relative dielectric constant of the medium between two plates. Since the area between two plates consists of Silicon rods and air, its correct value is calculated in the COMSOL environment. The electric field E can be expressed in terms of the total charge, ϵ and area is given in Equation 3.8

$$E = \frac{Q}{\epsilon A} \tag{3.8}$$

The force exerted between two plated under electric field can be found as in Equation 3.9,

$$F_{Total} = \left(\frac{Q}{2}\right) E$$
$$F_{Total} = \frac{Q^2}{2\epsilon A} \tag{3.9}$$

Any work done on the non-stationary plate (moving, pulling or lifting) can be expressed as distance d, the distance that the plate travels, as;

$$W(d) = Fd = \frac{Q^2 d}{2\epsilon A} \tag{3.10}$$

The stored potential energy W(Q) is given is Equation 3.11

$$W(Q) = \frac{Q^2}{2C} = \frac{Q^2 d}{2\epsilon A} \tag{3.11}$$

The force exerted between two plates can be found as in Equation 3.12.

$$dW = Fdz$$
$$F = \frac{Q^2}{2\epsilon A} \tag{3.10}$$

The initial air gap is calculated as 100 nm and it will be shrunk to a value near 5-10 nm. The structure is modeled in COMSOL since the analysis will be too complicated

for such a device with fringing fields and non-uniformly distributed varying dielectric constant materials inside the device. The device is modeled as a rectangular diaphragm with two rigid supports at each side and no built-in stress. The required voltage to pull the top plate to the desired distance is calculated as 4.96 V.

CHAPTER 4

EXPERIMENTAL VERIFICATION OF OPTICAL EXCITATION FOR PHC MACH-ZEHNDER INTERFEROMETER

This chapter summarizes the experimental studies for optical MZI modulators by optical excitation of the previously designed structures [52], [74]–[78]

4.1 2D PhC Mach-Zehnder Interferometer Based Modulator

In all of the wave domains, interference is one of the most important phenomena that when two waves encounter at the same medium, they interact with each other according to some defined principles. When an interference occurs, the resultant wave is just the superposition of those two waves. The most important interference types are constructive interference and destructive interference. In Figure 4.1, an example of interference patterns is presented. Figure 4.1**(a)** represents the destructive interference of two waves with a π-radian difference in their phases. They completely cancel out each other when the interference occurs. On the contrary, in Figure 4.1**(b)**, constructive interference patterns are presented where the two waves are in-phase (there aren't any phase difference) and the resultant wave is the sum of those two waves.

Mach-Zehnder interferometer(MZI) is an interferometer type that is both suitable for optics and integrated photonics due to its simplistic structure and relatively low footprint [79]. A typical MZI consists of two Y-branch beam splitters that first divide the incoming wave intensity into two equal parts at the input side. Those two waves propagate and accumulate different (or same) phases and the second Y-branch combines them equally at the output side. The MZI structures are generally designed to have constructive interference at the steady state and destructive interference at the excited state.

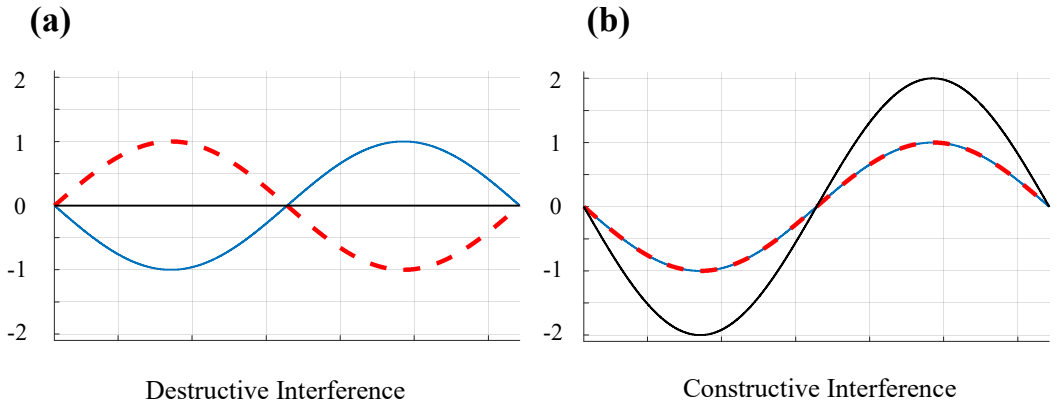

Figure 4.1. Illustration of interference patterns. The solid light blue line and dashed green line represent the two waves that undergo interference and the solid black line represents the resultant wave. **(a)** Destructive Interference **(b)** Constructive Interference.

The intensity at the output of an MZI can be calculated by assuming that if the initial E-field intensity E_0 is divided into two equal parts by the first Y-branch, E_1 and E_2. The intensity at the output can be expressed as the sum of those two intensities in terms of their accumulated phases ϕ ($\phi = n\frac{2\pi}{\lambda}L$). Then, the output intensity can be expressed as in Equation 4.1 as;

$$E_0 = E_1 e^{i\phi_1} + E_2 e^{i\phi_2} \tag{4.1}$$

To calculate the output intensity I the squared sum of the two E-field intensities are required as shown in Equation 4.2,

$$I_0 = |E_0|^2 = \left|E_1 e^{i\phi_1} + E_2 e^{i\phi_2}\right|^2$$
$$I_0 = \left|E_1 e^{i\phi_1}\right|^2 + \left|E_2 e^{i\phi_2}\right|^2 + E_1^* E_2 e^{-i\phi_1} e^{i\phi_2} + E_1 E_2^* e^{i\phi_1} e^{-i\phi_2} \tag{4.2}$$

where $\left|E_1 e^{i\phi_1}\right|^2$ and $\left|E_2 e^{i\phi_2}\right|^2$ are the intensities I_1 and I_2 in the arms of the MZI. Then, Equation 4.2 can be rearranged as;

$$I_0 = I_1 + I_2 + 2\sqrt{I_1 I_2}\cos\phi \tag{4.3}$$

where ϕ is the phase difference between two waves when they reach the output of the MZI. If we assume that the initial intensities are the same I_1=I_2=I, then the equations become,

$$I_0 = 2I(1 + \cos\phi) \quad (4.4)$$

The main goal is to create a π-radian phase shift with the smallest footprint, lowest power consumption, highest operation speed and bandwidth. There have been many remarkable studies on Silicon integrated PhC modulators, since PhC can be carefully engineered so that the same phase accumulation for a bare silicon waveguide can be achieved with a PhC structure on much shorter dimensions. Some of the smallest confirmed device size is 80 μm in length with an operation voltage of 2V for 1 Gb/s operation speed [80].

4.1.1 Numerical Analysis

To shrink the device size, we have implemented a novel band-to-band transition method to make the effective refractive index change from positive to negative [52]. This allows a π-radian phase accumulation with using a much shorter phase shifter region as stated nearly 5.5μm. The PhC structure is designed as a hexagonal lattice with a lattice constant *a* of 456nm. The structure is built on a SOI wafer with 260nm Silicon thickness on top of 2μm SiO_2. The air holes with a radius *r* of 0.224*a* are etched on the silicon wafer. The corresponding band diagram of such a structure for TM-like excitation is given in Figure 4.2**(a)**. As is shown, there are two plots on the same band diagram, the dashed blue line represents when the device is in off-state, meaning the bulk refractive index of the silicon is 3.48. The solid red lines represent the on-state where the bulk refractive index of the silicon is changed to 3.47. As it is shown in Figure 4.2**(b)**, the on and off state bands transition states at 1550 nm wavelength. The effective refractive index of the mode for 1550 nm wavelength changes from positive to negative. This transition changes the effective refractive index Δn_{eff} = -3.886, although the silicon refractive index changes by 0.01, since the transition happens from the effective refractive index of the mode for -1.89 to 1.996.

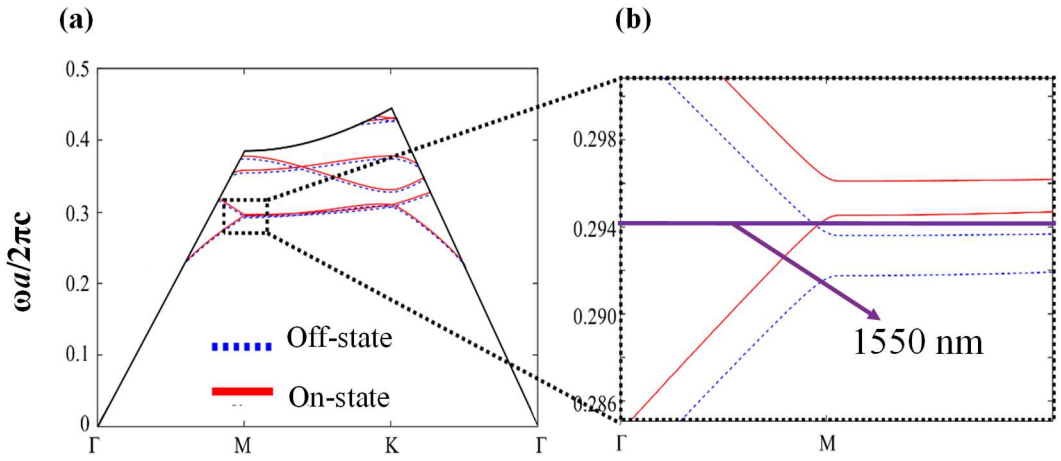

Figure 4.2 The band diagram for the 2D hexagonal lattice for band transition. The dashed blue line represents the off-state and the solid blue line represents the on-state.

The method of changing the refractive index of bulk Silicon is done with the plasma-dispersion effect. As the number of carriers increases in the region, its refractive index shifts and based on Soref and Bennett's work [51], the number of carriers required for Silicon to make a 0.01 shift in the refractive index is $4.1 \times 10^{-18} cm^{-3}$.

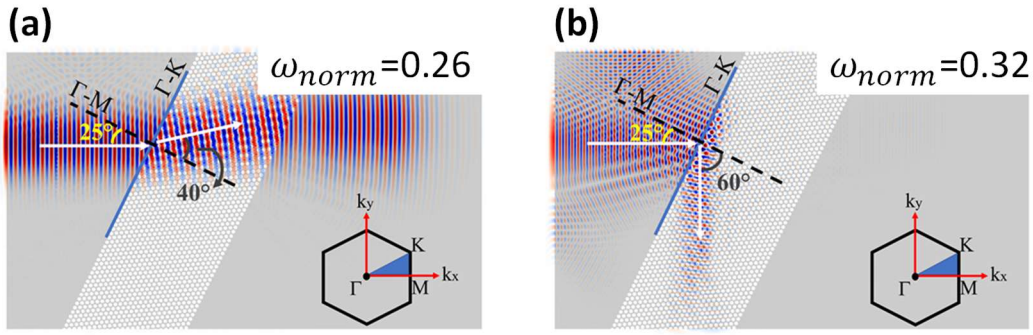

Figure 4.3 Observation of negative refractive index from mode profile. **(a)** Positive refraction. **(b)** Negative refraction. [52]

First, the effect of the negative refractive index should be observed so that Snell's Law would yield negative refraction with incident light. To observe this, a PhC with parameters with r=0.3a, h=0.6a and a=0.5 μm is created. Two lights with normalized frequencies of ω=0.26 and ω=0.32 are introduced to the PhC with an incidence angle of 25°. The results are shown in Figure 4.3 [52]. As expected, the incident light makes

a positive angle with the normal of the incidence boundary for the case when the normalized frequency is 0.26. However, for 0.32, the negative refraction occurs as it behaves very differently and makes a negative angle with the normal as shown in Figure 4.3**(b)**.

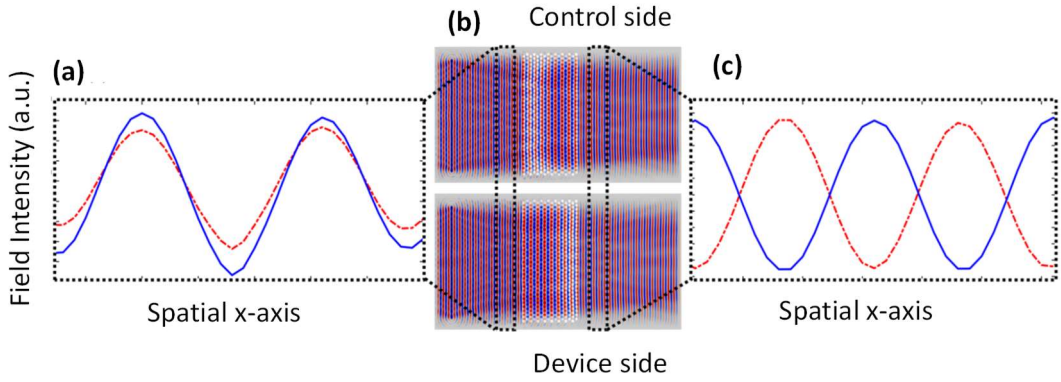

Figure 4.4. **(a)** Field intensity of the input signal for both arms. **(b)** The PhC structure and mode profile for the Control side and Device side. **(c)** The field intensities at the output side of both signals.[52]

The phase difference between both arms needs to be π-radians to successfully achieve the destructive interference for amplitude modulation. Even though the analysis from the band diagram confirms this phase shift, the exact field profile of the control arm, where the bulk index stays as 3.48 and the device arm, where the bulk index is changed to 3.47, need to be investigated. For this reason, two different simulations were performed by creating just the phase shifter parts of the MZI. The same input signal is applied to both of them and the phase difference at the output side is measured by extracting the E-field profile. The results of this simulation are given in Figure 4.4. In Figure 4.4**(a)** both signals have the same phase at the input side and in Figure 4.4**(b)** the mode profile of those signals is given on top of the PhC. Figure 4.4**(c)** shows that a π-radians phase shift is achieved on a relatively small region of PhCs.

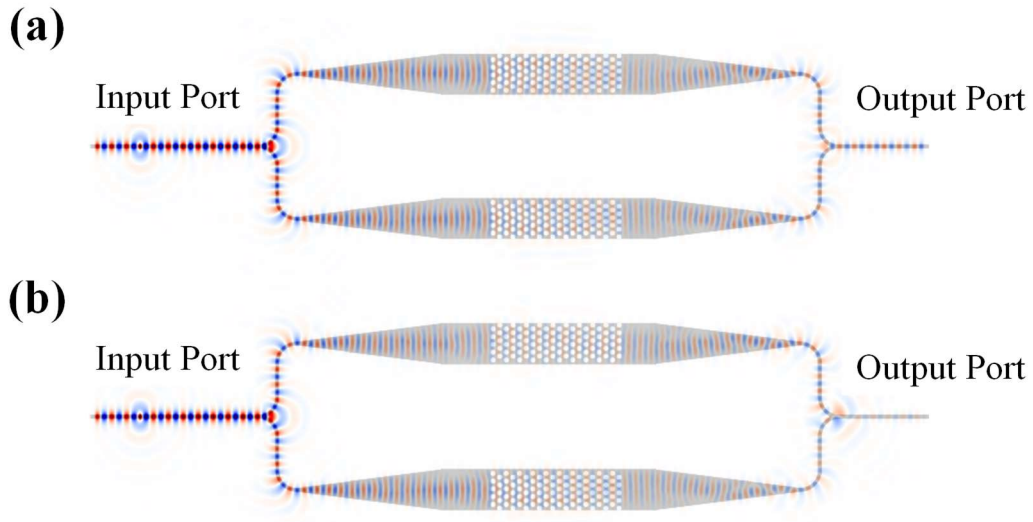

Figure 4.5. Mode profile of 2D PhC MZI. **(a)** Non excited state (off-state) **(b)** Excited state (on-state)

Then, the same structure is analyzed via 3D FDTD methods and its E-field profile is extracted for both on and off state to observe the E-field behavior when both arms are combined and an MZI structure is created. The resultant mode profiles for both states are presented in Figure 4.5, the waves on different arms of the MZI make a constructive interference at the output and E-field intensity is observed at the output port in Figure 4.5**(a)**. However, in Figure 4.5**(b)** the bulk silicon index of one arm is shifted from 3.48 to 3.47 which results in destructive interference occurs and there are no electric fields present at the output port.

4.2 Experimental Setup

The experiments were conducted in Middle East Technical University Integrated Photonics Laboratory. Some of the critical active components of the experimental setup are presented in Table 4.1. There are a lot of passive components used; however, the most important ones will be presented in a schematic in this part.

Table 4.1. List of active components and their models that were used for experimental characterization

Component Name	Model
Optical Spectrum Analyzer	Anritsu MS9740B
C&L Band ASE Light Source	ThorLabs ASE730
Tunable Semiconductor Laser	Santec TSL-550
Oscilloscope	Teledyne Lecroy Waverunner 8404
Signal Generator	Keysight 33220A
Optical Injection Laser	Laserglow LRS-0532
Vibrationless Optical Table	Thorlabs
Optical Illuminator	Edmund Optics MI-150
Visible Camera	Thorlabs Monochrome CMOS Camera
Infrared Camera	Sensors Unlimited,UTC & Natural Instruments
Optical Powermeter	Thorlabs PM100D

The simplified schematic of the experimental setup is presented in Figure 4.6. The input light source is first met with a linear polarizer than a polarization rotator. This enables to send both TE-like and TM-like sources whichever is required. Then, the light is focused onto the side of the waveguide, which is carefully cleaved and positioned, for coupling. The coupling is done with the help of taper-lens fibers, which have a focusing distance of 10 μm and sensitive micro-positioner stations while observing them from the infrared camera. Beam splitter cubes split the light into two halves in the direction of their partially transparent mirror. 50% of the light goes through the same direction which it came from and 50% of the light is reflected to according to the beam splitters' mirror position.

A flip mirror controls the direction of the light in this setup. If the flip mirror stands vertical (solid line in Figure 4.6), the image of the chip is directly going to the infrared camera. This is required for maximizing the coupling since the light sources

operate in the infrared region. An illuminator is used for the illumination of the chip when the infrared camera is operational.

When the flip mirror stands horizontal (dashed line in Figure 4.6), the image of the chip is redirected 90 degrees to the right side. There are a few important things in this configuration that need attention. Firstly, since the path to the infrared camera is blocked by the flip mirror, a second camera is needed to observe the chip. However, the only light source in this case is the Optical Excitation Laser which operates in the visible region with a 532 nm wavelength. Also, they should join on the same optical path to get an image of the chip, but since the required excitation power is too much so that it might cause a malfunction in the visible camera (which will be explained later in this chapter) so the path is divided with a beam splitter cube.

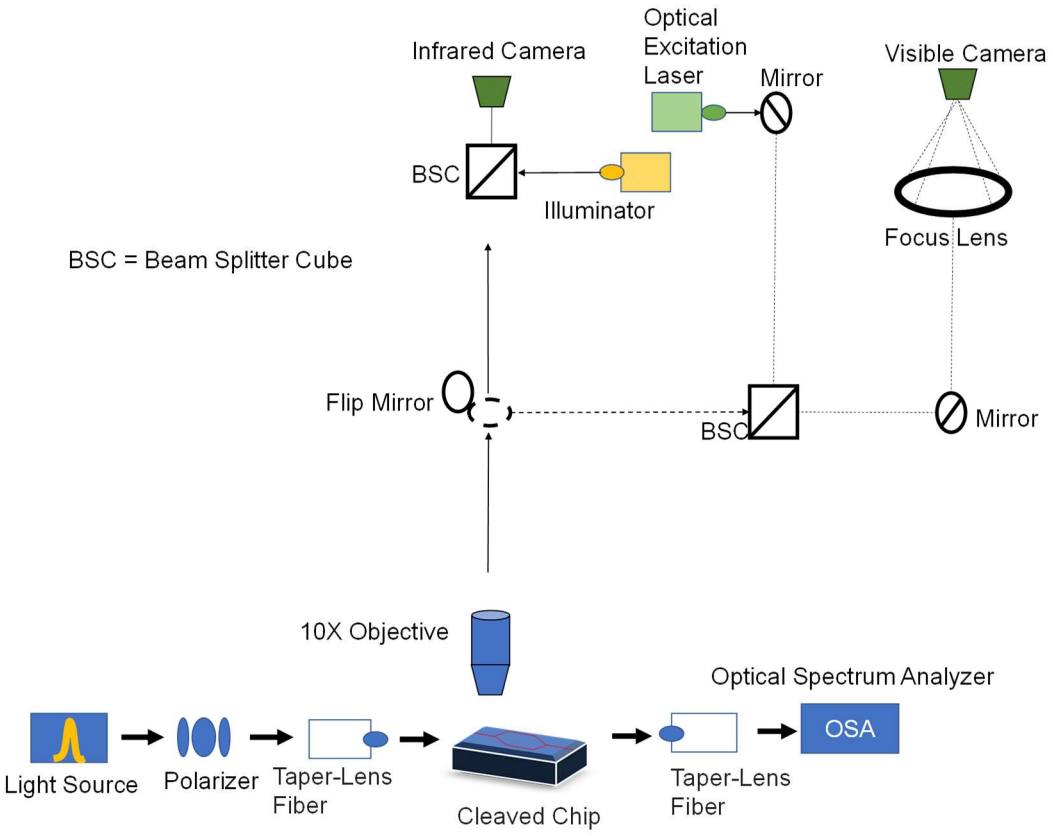

Figure 4.6. Schematic of the simplified version of the experimental setup

The dashed optical path in Figure 4.6 carries both the excitation laser for the chip and the image of the chip. The image of the chip is then redirected to the visible camera and focused on the camera with a convex lens. This procedure is done after coupling the input to the output, which is proceeded by the optical excitation of the chip and observing the output power. The excitation laser is focused on the chip via a 10X objective, precisely onto the PhC structure, so the index change is achieved by optical carrier injection. A picture of the experimental setup while conducting the optical carrier injection process is shown in Figure 4.7. Most of the components that are listed in Figure 4.6 can be seen in this figure except the light source and OSA.

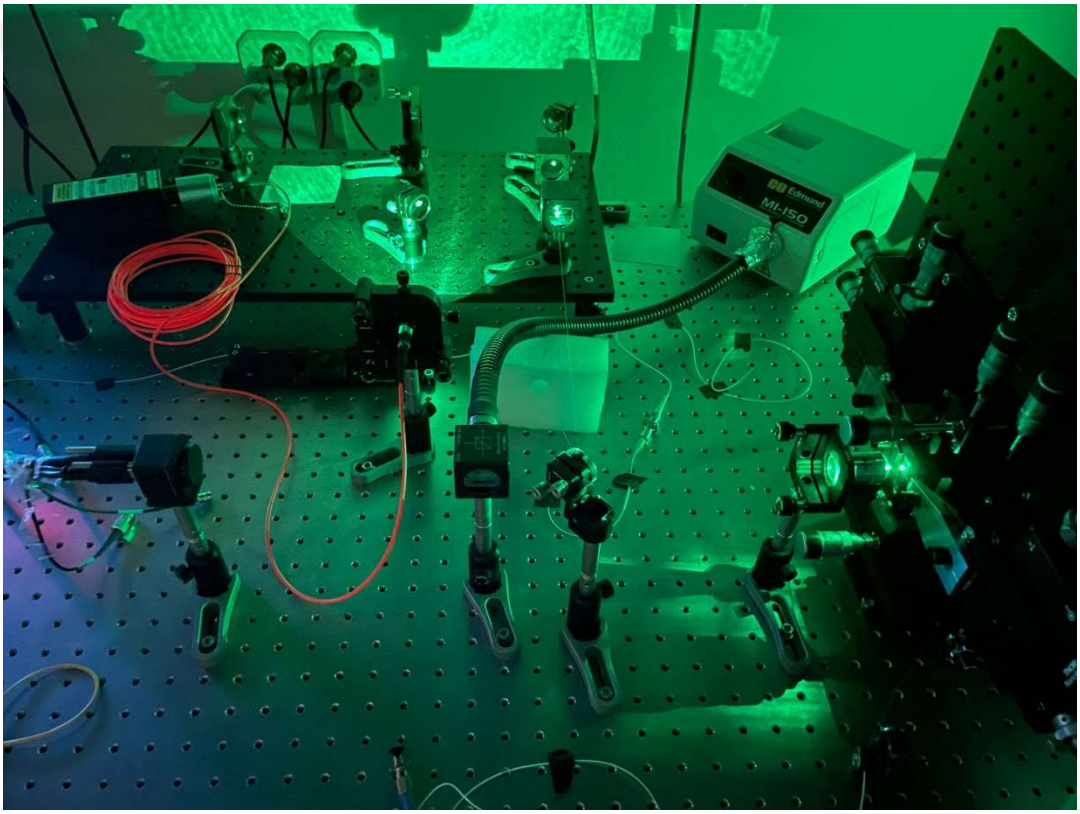

Figure 4.7. Experimental setup.

4.2.1 Fabrication and Measurements

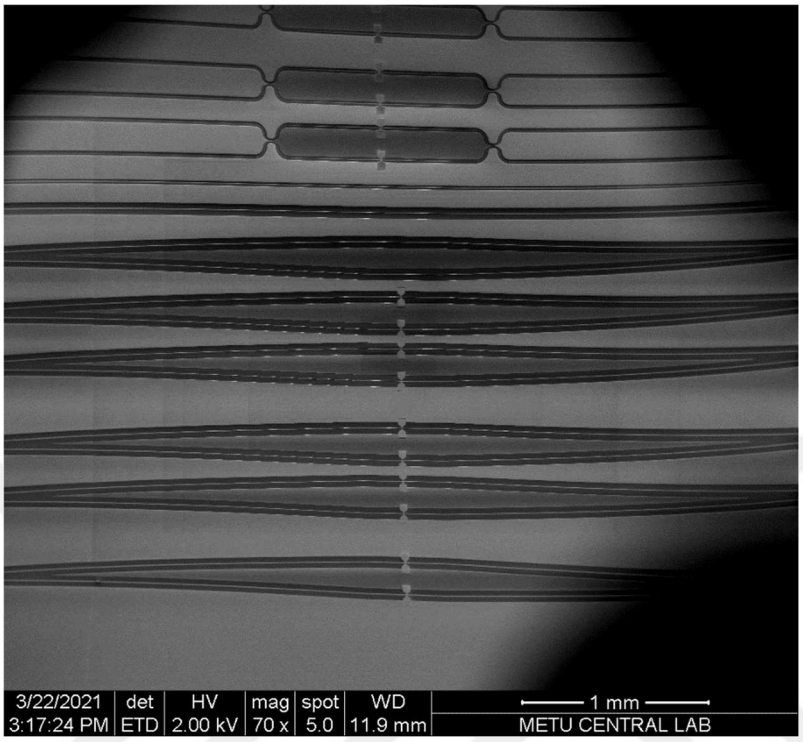

Figure 4.8. Zoomed out SEM Image of the fabricated chip

After the design and numerical analysis, the devices were fabricated with Electron-beam (E-beam) lithography on a 260 nm thick SOI wafer. First, the devices were sent to METU CENTRAL LAB for SEM Images of the devices, since a change in the PhC dimensions might dramatically alter the device characteristics. Since some variations are inevitable, a lot of different designs which have varying sizes were made and fabricated. A sample SEM image is shown in Figure 4.8. As it is seen from the figure that many devices with varying PhC dimensions were fabricated to minimize the fabrication errors. The layout of one of the designed 2D PhC structures is given in Figure 4.9**(a)**, and a zoomed-in image of the PhC structure is also shown in Figure 4.9**(b)**. Due to the variations in the fabrication, the radius of the air holes was nearly 1.5 times bigger than the designed ones in the initial layouts.

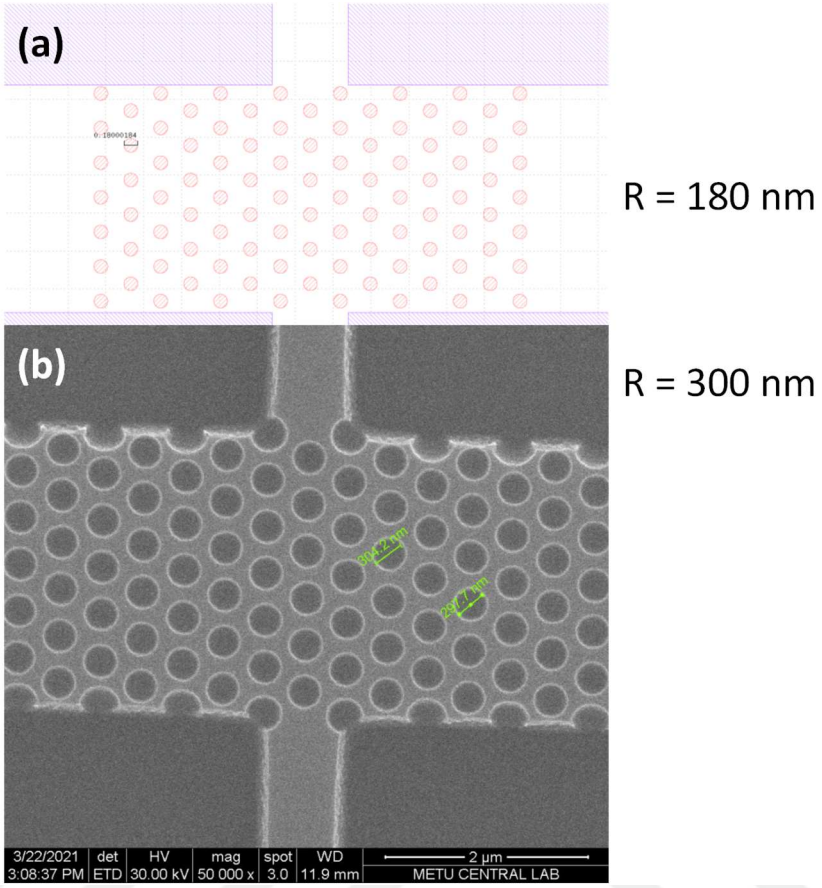

Figure 4.9. **(a)** The layout of the designed PhC structure. **(b)** SEM image of PhC part of the MZI.

After a series of parameter scans in designs and micro-fabrication steps, four of the configurations are shown in Figure 4.10, structures with the desired dimensions have been fabricated and the measurements were conducted with them.

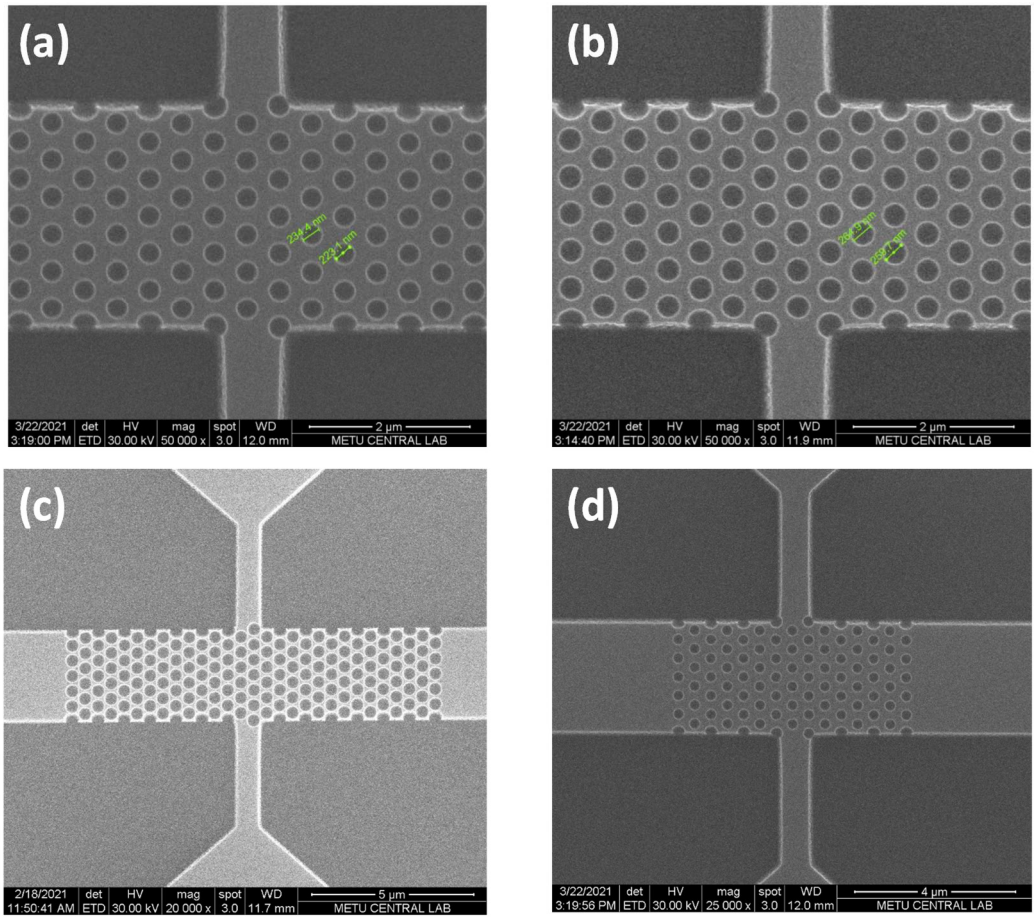

Figure 4.10.**(a),(b),(c),(d)** SEM image of various sized PhC structures.

First, the transmission spectrum of each device is extracted and a band gap is tried to be found by using a broadband light source. Then, the devices with the desired parameters were chosen (which have a band gap around 1550 nm wavelength), then those devices were thoroughly analyzed with different polarization configurations. After that the light source is changed to a single wavelength laser and the optical carrier injection was carried out for selected devices. A signal generator modulates the injection laser with an appropriate square wave with 50% duty cycle and 1 and 2 kHz frequencies. Then the output signal is read by the optical power meter which converts the optical signal to an electrical signal and its output is also connected to an oscilloscope.

To make sure that there exist a band gap in the fabricated PhC devices, additional waveguides with PhC structures were also fabricated to characterize of both arms of MZI structures. They are used for only one purpose, finding the exact location of the band gap on the spectrum. Since the extraction and numerical analysis of a band diagram structure assumes that there are infinitely many number of unit cells, however in reality it is impossible. However, if the length of the PhC structure is optimized so that there are sufficiently many number of unit cells, a band gap can be observed. In Figure 4.11, this exact case can be seen. Transmission spectra from two devices were obtained, where every property except the number of unit cells is different. One has fewer air holes than the other. The existence of the band gap is clearly seen in the longer PhC.

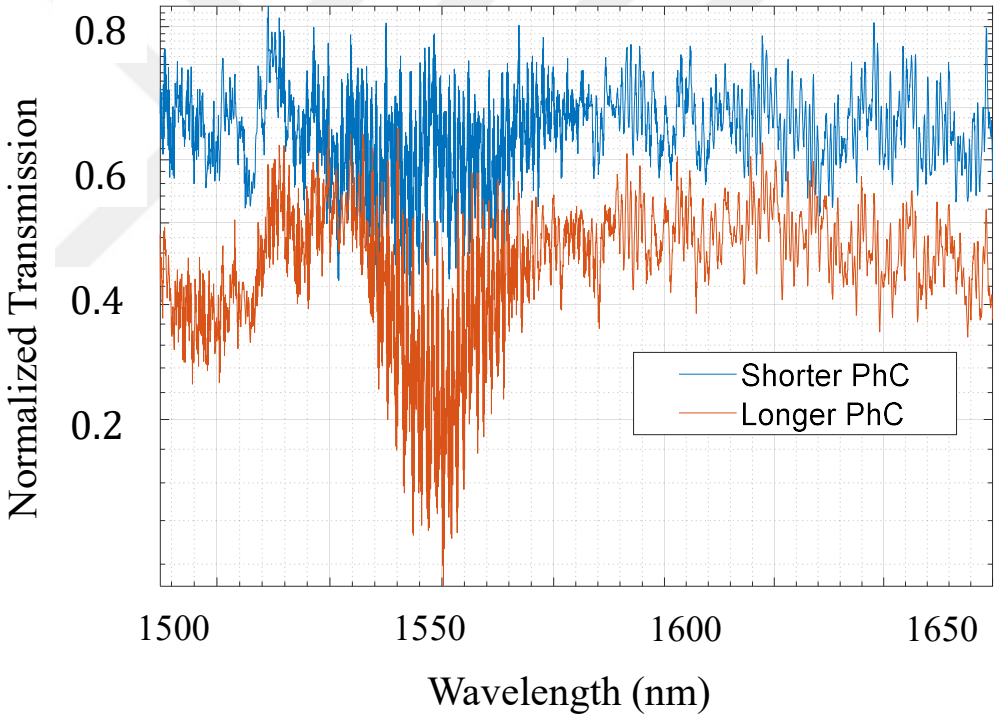

Figure 4.11. Transmission spectrum from PhC structure with r=160 nm. The blue line represents the short PhC structure (which has less number of unit cells in the direction of the propagation), the orange line represents the longer PhC where band gap is clearly seen around 1550 nm wavelength.

The MZI structure then went into the optical excitation process for modulating the output intensity. The optical carrier injection laser was modulated via a signal generator with 2 kHz square wave signal, when the light source for the chip is a single wavelength laser operating at 1549.53 nm wavelength. The output is connected to the detector and measured with an oscilloscope. Then, the modulation of the output light intensity is captured as shown in Figure 4.12. The blue line represents the measured output light intensity converted to an electrical signal by the detector. The modulation signal was recreated and put as a reference.

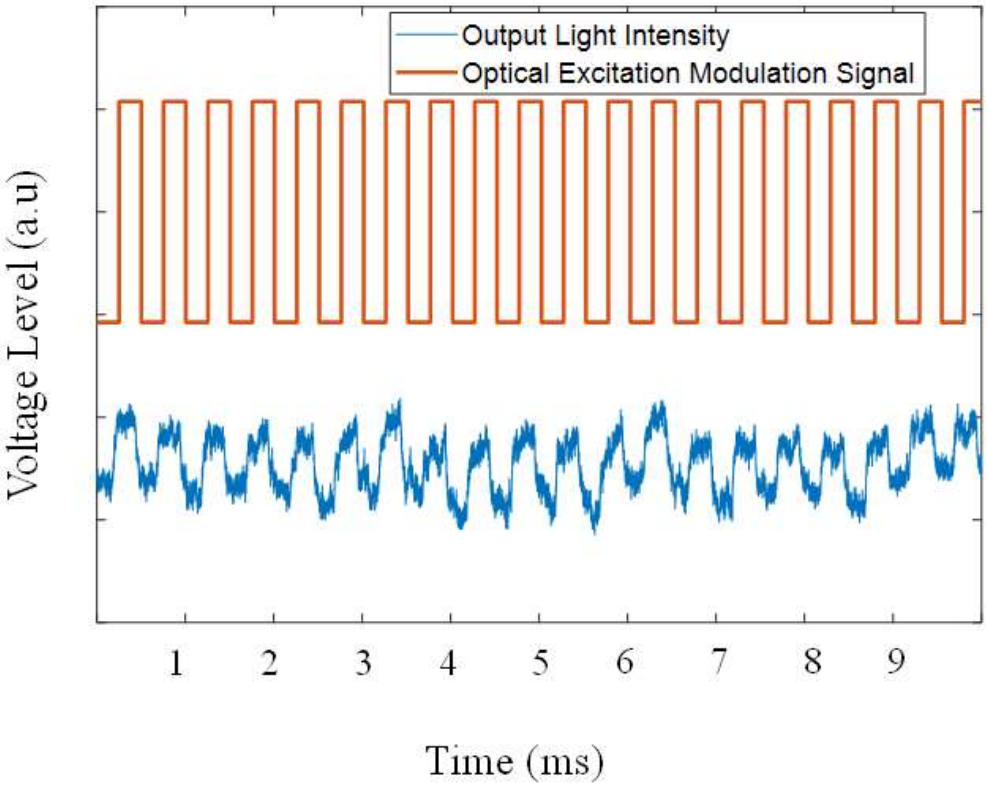

Figure 4.12. Intensity modulation of the MZI with optical carrier injection.

The optical injection laser has a maximum drive frequency of 2 kHz, so the experiments were done with 2 kHz modulation as seen in Figure 4.12. The conceptual confirmation of the modulation is done and the optical modulation with respect to the input signal is successfully achieved from the optical output signal.

This was done with the all optical modulation without any electrical connections present on the experimental setup.

CHAPTER 5

CONCLUSION AND FUTURE OUTLOOK

We have proposed the first highly tunable 2D rod-type PhC cavity for a refractive index sensing application. The light confinement was achieved by sandwiching the rods between two PEC layers (which are replaced by gold) to make the effective rod heights as infinity. The structure also has an internal electrical tuning mechanism by applying a voltage to two metal plates and carefully positioning them via electrostatic actuation. Since the E-field is heavily confined in a small region in the air gap on top of the rods near the cavity, the resonance characteristics are heavily dependent on the size of the air gap. By utilizing electrostatic actuation, the size of the air gap is first pulled to an appropriate value after fabrication, then it is calibrated to have a resonance wavelength at 1550 nm. Fano-resonance is utilized for creating resonance characteristics that is more suitable for detection instead of Lorentzian characteristics since the transmission depth is larger as well as Q-factor. However, the maximum transmission is reduced by 3 dB since the rod in the middle of the waveguide. It is shown that even with a relatively low Q-factor, a very small detection limit can be achieved with high sensitivity and Fano-like resonance. Strong localization of the E-field in the air region creates the opportunity for simple and reliable tuning of the cavity resonance, which paves the way for many sensing applications and decreases the effect of fabrication errors. A comparison table with similar devices in the literature is given in Table 5.1. The mode-volume of this device is calculated as 0.214 $(\lambda/n)^3$ and sub-wavelength confinement is achieved without utilizing a nanobeam-cavity like conventional designs. The internal tuning mechanism offers great versatility and minimizes the fabrication errors, as well as the design can stay the same but can operate at a relatively broad spectrum of 50 nm around 1550 nm wavelength. The design points at a novel, simple and effective way of optical-sensing and can be used for many applications, sensing, detection, and classification of gases,

airborne molecules, and pathogenic micro-organisms.

Table 5.1 Comparison of Device Performance Metrics with Literature

Reference	Sensitivity (nm/RIU)	Q-Factor	S/FWHM	Tuning Range (nm)
Jágerská *et al* [21]	510	25000	8069	-
Sünner *et al* [71]	83.3	40000	2064	-
Mohamed *et al* [81]	422	549	149.5	-
Tang *et al* [82]	1125	102.4	74	-
Wang *et al* [83]	233	70000	10522	-
Mohammad and Behnam [84]	720	30	14	-
This Work	1039	2242	748	50.4

The design stands as the first PhC tunable biosensor. Although the numerical analysis and confirmation of the device performance with various simulation methods are conducted, the device is yet to be fabricated and experimental analysis is not completed. Thus, firstly, the design will be fabricated using one of the confirmed design method from [70], then it will be analyzed. The resonance and transmission characteristics will be measured, then the tuning mechanism will be investigated by precisely applying voltage to avoid pull-in. The main difficulty of the fabrication is the inherent loss that will be introduced by gold should be minimized since it will be the main loss mechanism in the device. The experimental setup that is described in Chapter 4 will be used for characterization.

For the second part of this thesis, the experimental confirmation of the optical modulation for the MZI structure is achieved with the optical carrier injection method. PhC band diagram is designed so that the dielectric band and air band are very close to each other and with a slight shift of the bulk refractive index, the modes with some certain frequencies can be transitioned from first band to the second band,

and that would result in a much larger phase accumulation and π-radian phase shift is achieved in a smaller region. By benefitting from the negative refractive index and negative phase accumulation the effective refractive index difference between on and off states were calculated as Δn_{eff} = -3.886 even though the bulk silicon index is shifted from 3.48 to 3.47. Thus, the intensity modulation is achieved with a much smaller phase shifter length compared to the ones in the literature (~5 μm). Currently, performance characteristics have been optimized by adjusting design with the experimental feedback.

For future work, photonic structures discussed here will be co-integrated with the other active and passive components that are also developed in our group such as various photodetector designs [85]–[89], quantum information processing applications [90]–[93] and novel structures [94]–[96] in order to support the effort for all optical photonic network on the same chip both in classical and quantum regimes.

REFERENCES

[1] H. Xu, P. Wu, C. Zhu, A. Elbaz, and Z. Z. Gu, "Photonic crystal for gas sensing," *J. Mater. Chem. C*, 2013.

[2] Y. Chen *et al.*, "Label-free biosensing using cascaded double-microring resonators integrated with microfluidic channels," *Opt. Commun.*, 2015.

[3] N. Cohen, P. Sabhachandani, A. Golberg, and T. Konry, "Approaching near real-time biosensing: Microfluidic microsphere based biosensor for real-time analyte detection," *Biosens. Bioelectron.*, 2015.

[4] J. D. Joannopoulos, S. G. Johnson, J. N. Winn, and R. D. Meade, *Photonic crystals: Molding the flow of light*. 2011.

[5] J. Kirchhof *et al.*, "Photonic crystal fibers," in *Photonic Crystals: Advances in Design, Fabrication, and Characterization*, 2006.

[6] Y. Akahane, T. Asano, B. S. Song, and S. Noda, "High-Q photonic nanocavity in a two-dimensional photonic crystal," *Nature*, 2003.

[7] H. G. Park, C. J. Barrelet, Y. Wu, B. Tian, F. Qian, and C. M. Lieber, "A wavelength-selective photonic-crystal waveguide coupled to a nanowire light source," *Nat. Photonics*, 2008.

[8] I. A. Sukhoivanov and I. V. Guryev, "Photonic crystal waveguides," *Springer Ser. Opt. Sci.*, 2010.

[9] Y. Akahane, T. Asano, B.-S. Song, and S. Noda, "Fine-tuned high-Q photonic-crystal nanocavity," *Opt. Express*, 2005.

[10] F. Q. Shi, Y. Y. Luo, D. R. Chen, J. J. Chen, Z. J. Ren, and B. J. Peng, "A dual-parameter sensor based on the asymmetry of alcohol filling the photonic crystal fiber in sagnac loop," *IEEE Sens. J.*, 2018.

[11] R. Ge, J. Xie, B. Yan, E. Liu, W. Tan, and J. Liu, "Refractive index sensor

with high sensitivity based on circular photonic crystal," *J. Opt. Soc. Am. A*, 2018.

[12] A. Shi, R. Ge, and J. Liu, "Refractive index sensor based on photonic quasi-crystal with concentric ring microcavity," *Superlattices Microstruct.*, 2019.

[13] Y. Jiang, W. Jiang, L. Gu, X. Chen, and R. T. Chen, "80-micron interaction length silicon photonic crystal waveguide modulator," *Appl. Phys. Lett.*, 2005.

[14] S. Kocaman, X. Yang, J. F. McMillan, M. B. Yu, D. L. Kwong, and C. W. Wong, "Observations of temporal group delays in slow-light multiple coupled photonic crystal cavities," *Appl. Phys. Lett.*, 2010.

[15] S. Kocaman *et al.*, "Observation of zeroth-order band gaps in negative-refraction photonic crystal superlattices at near-infrared frequencies," *Phys. Rev. Lett.*, 2009.

[16] T. Gu *et al.*, "Deterministic integrated tuning of multicavity resonances and phase for slow-light in coupled photonic crystal cavities," *Appl. Phys. Lett.*, 2011.

[17] S. Kocaman, M. S. Aras, N. C. Panoiu, M. Lu, and C. W. Wong, "On-chip optical filters with designable characteristics based on an interferometer with embedded silicon photonic structures," *Opt. Lett.*, 2012.

[18] S. C. Kilic and S. Kocaman, "Highly Sensitive and Tunable Fano-Like Rod-Type Silicon Photonic Crystal Refractive Index Sensor," *IEEE Sens. J.*, 2021.

[19] O. E. Orsel, M. Erdil, and S. Kocaman, "A 2D Slotted Rod Type PhC Cavity Inertial Sensor Design for Impact Sensing," *IEEE J. Quantum Electron.*, 2020.

[20] S. Moradi, A. Govdeli, and S. Kocaman, "Zero average index design via perturbation of hexagonal photonic crystal lattice," *Opt. Mater. (Amst).*,

2017.

[21] J. Jágerská, H. Zhang, Z. Diao, N. Le Thomas, and R. Houdré, “Refractive index sensing with an air-slot photonic crystal nanocavity,” *Opt. Lett.*, 2010.

[22] N. M. Iverson *et al.*, “In vivo biosensing via tissue-localizable near-infrared-fluorescent single-walled carbon nanotubes,” *Nat. Nanotechnol.*, 2013.

[23] J. N. Anker, W. P. Hall, O. Lyandres, N. C. Shah, J. Zhao, and R. P. Van Duyne, “Biosensing with plasmonic nanosensors,” *Nature Materials*. 2008.

[24] K. Debnath, K. Welna, M. Ferrera, K. Deasy, D. G. Lidzey, and L. O’Faolain, “Highly efficient optical filter based on vertically coupled photonic crystal cavity and bus waveguide,” *Opt. Lett.*, 2013.

[25] I. W. Frank, P. B. Deotare, M. W. McCutcheon, and M. Lončar, “Programmable photonic crystal nanobeam cavities,” *Opt. Express*, 2010.

[26] J. R. Mejía-Salazar and N. Porras-Montenegro, “Zero- $\bar{n}$ band gap in two-dimensional metamaterial photonic crystals,” *Superlattices Microstruct.*, 2015.

[27] T. Alexoudi, G. T. Kanellos, and N. Pleros, “Optical RAM and integrated optical memories: a survey,” *Light: Science and Applications*. 2020.

[28] S. Kocaman *et al.*, “Zero phase delay in negative-refractive-index photonic crystal superlattices,” *Nat. Photonics*, 2011.

[29] D. Dorfner *et al.*, “Photonic crystal nanostructures for optical biosensing applications,” *Biosens. Bioelectron.*, 2009.

[30] Q. Tan *et al.*, “Development of an optical gas leak sensor for detecting ethylene, dimethyl ether and methane,” *Sensors (Switzerland)*, 2013.

[31] K. Zandi, J. A. Belanger, and Y. A. Peter, “Design and demonstration of an in-plane silicon-on-insulator optical MEMS fabry-pérot-based accelerometer integrated with channel waveguides,” *J. Microelectromechanical Syst.*, vol.

21, no. 6, pp. 1464–1470, 2012.

[32] D. K. C. Wu, B. T. Kuhlmey, and B. J. Eggleton, “Ultra-sensitive photonic crystal fiber refractive index sensor,” in *2009 Conference on Lasers and Electro-Optics and 2009 Conference on Quantum Electronics and Laser Science Conference, CLEO/QELS 2009*, 2009.

[33] A. Iadicicco, S. Campopiano, A. Cutolo, M. Giordano, and A. Cusano, “Refractive index sensor based on microstructured fiber Bragg grating,” *IEEE Photonics Technol. Lett.*, 2005.

[34] S. Zou, F. Wang, R. Liang, L. Xiao, and M. Hu, “A nanoscale refractive index sensor based on asymmetric plasmonic waveguide with a ring resonator: A review,” *IEEE Sens. J.*, 2015.

[35] N. Skivesen, A. Têtu, M. Kristensen, J. Kjems, L. H. Frandsen, and P. I. Borel, “Photonic-crystal waveguide biosensor,” *Opt. Express*, 2007.

[36] J. Flueckiger *et al.*, “Sub-wavelength grating for enhanced ring resonator biosensor,” *Opt. Express*, 2016.

[37] M. R. Foreman, J. D. Swaim, and F. Vollmer, “Whispering gallery mode sensors,” *Adv. Opt. Photonics*, 2015.

[38] F. Vollmer and S. Arnold, “Whispering-gallery-mode biosensing: Label-free detection down to single molecules,” *Nat. Methods*, 2008.

[39] C. Li, B. Yan, and J. Liu, “Refractive index sensing characteristics in a D-shaped photonic quasi-crystal fiber sensor based on surface plasmon resonance,” *J. Opt. Soc. Am. A*, 2019.

[40] Y. Geng, L. Wang, X. Tan, Y. Xu, X. Hong, and X. Li, “A Compact Four-Wave Mixing-Based Temperature Fiber Sensor with Partially Filled Photonic Crystal Fiber,” *IEEE Sens. J.*, 2019.

[41] N. Erim, M. N. Erim, and H. Kurt, “An Optical Sensor Design Using

Surface Modes of Low-Symmetric Photonic Crystals," *IEEE Sens. J.*, 2019.

[42] A. Shi, R. Ge, and J. Liu, "Side-coupled liquid sensor and its array with magneto-optical photonic crystal," *J. Opt. Soc. Am. A*, 2020.

[43] T. Munoz-Hernandez, E. Reyes-Vera, and P. Torres, "Temperature Sensor Based on Whispering Gallery Modes of Metal-Filled Side-Hole Photonic Crystal Fiber Resonators," *IEEE Sens. J.*, 2020.

[44] B. T. Cunningham, M. Zhang, Y. Zhuo, L. Kwon, and C. Race, "Recent Advances in Biosensing with Photonic Crystal Surfaces: A Review," *IEEE Sens. J.*, 2016.

[45] D. Threm, Y. Nazirizadeh, and M. Gerken, "Photonic crystal biosensors towards on-chip integration," *Journal of Biophotonics*. 2012.

[46] W. A. Gambling, "The rise and rise of optical fibers," *IEEE J. Sel. Top. Quantum Electron.*, 2000.

[47] A. Shacham, K. Bergman, and L. P. Carloni, "Photonic networks-on-chip for future generations of chip multiprocessors," *IEEE Trans. Comput.*, 2008.

[48] A. L. Gaeta, M. Lipson, and T. J. Kippenberg, "Photonic-chip-based frequency combs," *Nature Photonics*. 2019.

[49] M. Melnichuk and L. T. Wood, "Direct Kerr electro-optic effect in noncentrosymmetric materials," *Phys. Rev. A - At. Mol. Opt. Phys.*, 2010.

[50] R. A. Norwood, C. T. Derose, C. Greenlee, and A. Yeniay, "Organic waveguides, ultra-low loss demultiplexers and electro-optic (EO) polymer devices," in *Handbook of Organic Materials for Optical and (Opto)Electronic Devices: Properties and Applications*, 2010.

[51] R. A. Soref and B. R. Bennett, "Electrooptical effects in silicon," *IEEE Journal of Quantum Electronics*. 1987.

[52] A. Govdeli, M. C. Sarihan, U. Karaca, and S. Kocaman, "Integrated Optical

Modulator Based on Transition between Photonic Bands," *Sci. Rep.*, 2018.

[53] S. C. Kilic and S. Kocaman, "High Sensitivity Fano-Like Rod-Type Silicon Photonic Crystal Refractive Index Sensor," in *2020 14th International Congress on Artificial Materials for Novel Wave Phenomena, Metamaterials 2020*, 2020.

[54] C. R. Pollock and M. Lipson, *Integrated Photonics. 2003.* .

[55] E. Yablonovitch, "Inhibited spontaneous emission in solid-state physics and electronics," *Phys. Rev. Lett.*, 1987.

[56] S. John, "Strong localization of photons in certain disordered dielectric superlattices," *Phys. Rev. Lett.*, 1987.

[57] S. G. Johnson and J. D. Joannopoulos, "Introduction to Photonic crystals: Bloch's theorem, band diagrams, and Gaps (but no defects)," *Photonic Cryst. Tutor.*, 2003.

[58] "MPB Documentation, Mpb.readthedocs.io, 2020."

[59] A. F. Oskooi, D. Roundy, M. Ibanescu, P. Bermel, J. D. Joannopoulos, and S. G. Johnson, "Meep: A flexible free-software package for electromagnetic simulations by the FDTD method," *Comput. Phys. Commun.*, 2010.

[60] E. DICKINSON, H. EKSTRÖM, and E. FONTES, "COMSOL Multiphysics," *Electrochem. commun.*, 2014.

[61] M. Erdil, Y. Ozer, and S. Kocaman, "High-Q slot-mode photonic crystal nanobeam cavity biosensor with optomechanically enhanced sensitivity," *IEEE J. Sel. Top. Quantum Electron.*, 2019.

[62] C. Feng, G. Y. Feng, N. J. Chen, and S. H. Zhou, "Ultrahigh-Q small-V photonic crystal nanobeam cavities based on parabolic-shaped width and taper holes," *Wuli Xuebao/Acta Phys. Sin.*, 2012.

[63] S. Makino, Y. Ishizaka, K. Saitoh, and M. Koshiba, "Slow-light-enhanced

nonlinear characteristics in slot waveguides composed of photonic crystal nanobeam cavities," *IEEE Photonics J.*, 2013.

[64] S. Y. Lin *et al.*, "A three-dimensional photonic crystal operating at infrared wavelengths," *Nature*, 1998.

[65] C. W. Chen *et al.*, "Large three-dimensional photonic crystals based on monocrystalline liquid crystal blue phases," *Nat. Commun.*, 2017.

[66] S. Fan, "Photonic Crystal Theory: Temporal Coupled-Mode Formalism," *Opt. Fiber Telecommun. V1A*, pp. 431–454, 2008.

[67] M. F. Limonov, M. V. Rybin, A. N. Poddubny, and Y. S. Kivshar, "Fano resonances in photonics," *Nat. Photonics*, 2017.

[68] W. M. Zhang, H. Yan, Z. K. Peng, and G. Meng, "Electrostatic pull-in instability in MEMS/NEMS: A review," *Sensors and Actuators, A: Physical*. 2014.

[69] Q. Quan *et al.*, "Single particle detection in CMOS compatible photonic crystal nanobeam cavities," *Opt. Express*, vol. 21, no. 26, p. 32225, 2013.

[70] Y. Li *et al.*, "On-chip zero-index metamaterials," *Nat. Photonics*, 2015.

[71] T. Sünner *et al.*, "Photonic crystal cavity based gas sensor," *Appl. Phys. Lett.*, 2008.

[72] M. Quan, J. Tian, and Y. Yao, "Ultra-high sensitivity Fabry–Perot interferometer gas refractive index fiber sensor based on photonic crystal fiber and Vernier effect," *Opt. Lett.*, 2015.

[73] A. Pannipitiya, I. D. Rukhlenko, M. Premaratne, H. T. Hattori, and G. P. Agrawal, "Improved transmission model for metal-dielectric-metal plasmonic waveguides with stub structure," *Opt. Express*, 2010.

[74] A. Gövdeli, "Integrated optical modulators based on photonic crystals," Middle East Technical University, 2018.

[75] A. Govdeli and S. Kocaman, “On-Chip Switch and Add/Drop Multiplexer Design with Left-Handed Behavior in Photonic Crystals,” *IEEE J. Sel. Top. Quantum Electron.*, 2020.

[76] A. Gövdeli, S. Kocaman, and M. Erdil, “Tunable integrated optical modulator with dynamical photonic band transition of photonic crystals,” 2019.

[77] M. Yildirim, A. Gövdeli, and S. Kocaman, “Integrated optical modulators with zero index metamaterials based on photonic crystal slab waveguides,” 2019.

[78] A. Govdeli, M. C. Sarihan, U. Karaca, and S. Kocaman, “Band-to-Band Transition Based On-Chip Optical Modulator,” in *31st Annual Conference of the IEEE Photonics Society, IPC 2018*, 2018.

[79] H. Saghaei, P. Elyasi, and R. Karimzadeh, “Design, fabrication, and characterization of Mach–Zehnder interferometers,” *Photonics Nanostructures - Fundam. Appl.*, 2019.

[80] Y. Hinakura, Y. Terada, T. Tamura, and T. Baba, “Wide spectral characteristics of Si photonic crystal Mach-Zehnder modulator fabricated by complementary metal-oxide-semiconductor process,” *Photonics*, 2016.

[81] M. S. Mohamed, M. F. O. Hameed, N. F. F. Areed, M. M. El-Okr, and S. S. A. Obayya, “Analysis of highly sensitive photonic crystal biosensor for glucose monitoring,” *Appl. Comput. Electromagn. Soc. J.*, 2016.

[82] Y. Tang *et al.*, “Refractive index sensor based on fano resonances in metal-insulator-metal waveguides coupled with resonators,” *Sensors (Switzerland)*, 2017.

[83] C. Wang *et al.*, “High figure of merit ultra-compact 3-channel parallel-connected photonic crystal mini-hexagonal-H1 defect microcavity sensor array,” *Opt. Commun.*, 2017.

[84] D. Mohammad and K. Behnam, “Design of a label-free photonic crystal refractive index sensor for biomedical applications,” *Photonics Nanostructures - Fundam. Appl.*, 2018.

[85] F. Uzgur, U. Karaca, E. Kizilkan, and S. Kocaman, “All InGaAs Unipolar Barrier Infrared Detectors,” *IEEE Trans. Electron Devices*, 2018.

[86] M. H. Dolas and S. Kocaman, “Fully Depleted InP Nano-Layer for In-Device Passivation of InGaAs SWIR Detectors,” *IEEE Electron Device Lett.*, 2017.

[87] Y. Ozer and S. Kocaman, “Generation recombination suppression via depletion engineered heterojunction for alternative substrate MWIR HgCdTe infrared photodetectors,” *J. Appl. Phys.*, 2017.

[88] K. Circir, M. H. Dolas, and S. Kocaman, “Optimization of in-device depleted passivation layer for InGaAs photodetectors,” *Infrared Phys. Technol.*, 2019.

[89] F. Uzgur, U. Karaca, E. Kizilkan, and S. Kocaman, “Al/Sb free InGaAs unipolar barrier infrared detectors,” in *Infrared Technology and Applications XLIII*, 2017.

[90] and C. W. W. Xiang Cheng, Zhenda Xie, Kai-Chi Chang, Murat Can Sarihan, Yoo Seung Lee, Abhinav Kumar Vinod, Yongnan Li, XinAn Xu, Serdar Kocaman, Mingbin Yu, Dim-Lee Kwong, Jeffrey H. Shapiro, Franco N. C. Wong, “Quantum State Tomography of an On-chip Polarization-Spatial Qubit SWAP Gate,” 2021.

[91] A. B. Bozkurt and S. Kocaman, “On-chip deterministic optical SWAP gate,” 2019.

[92] A. Tugen and S. Kocaman, “Quantitative analysis of nonlinear dynamics of quantum light transmission in strongly coupled quantum dot-cavity systems,” *Opt. Commun.*, 2019.

[93] S. Kocaman and G. T. Sayan, “Comparison of coherently coupled multi-cavity and quantum dot embedded single cavity systems,” *Opt. Express*, 2016.

[94] U. Karaca, A. Govdeli, and S. Kocaman, “Hybrid Integration of Broadband Silicon Modulators and InGaAs Photodetectors,” in *31st Annual Conference of the IEEE Photonics Society, IPC 2018*, 2018.

[95] Y. Ozer and S. Kocaman, “Stability Formulation for Integrated Opto-mechanic Phase Shifters,” *Sci. Rep.*, 2018.

[96] M. C. Sarihan *et al.*, “Flexible waveguides with amorphous photonic materials,” 2019.